
Doctoral Dissertations

Student Theses and Dissertations

Summer 2017

Studies on neutron diffraction and X-ray radiography for material inspection

Fahima Fahmida Islam

Follow this and additional works at: https://scholarsmine.mst.edu/doctoral_dissertations



Part of the [Nuclear Engineering Commons](#)

Department: Mining and Nuclear Engineering

Recommended Citation

Islam, Fahima Fahmida, "Studies on neutron diffraction and X-ray radiography for material inspection" (2017). *Doctoral Dissertations*. 2597.

https://scholarsmine.mst.edu/doctoral_dissertations/2597

This thesis is brought to you by Scholars' Mine, a service of the Missouri S&T Library and Learning Resources. This work is protected by U. S. Copyright Law. Unauthorized use including reproduction for redistribution requires the permission of the copyright holder. For more information, please contact scholarsmine@mst.edu.

STUDIES ON NEUTRON DIFFRACTION AND X-RAY RADIOGRAPHY FOR
MATERIAL INSPECTION

by

FAHIMA FAHMIDA ISLAM

A DISSERTATION

Presented to the Faculty of the Graduate School of the
MISSOURI UNIVERSITY OF SCIENCE AND TECHNOLOGY

In Partial Fulfillment of the Requirements for the Degree

DOCTOR OF PHILOSOPHY

in

NUCLEAR ENGINEERING

2017

Approved
Hyoung K. Lee, Advisor
Ayodeji B. Alajo
Xin Liu
Joshua P. Schlegel
Randy H. Moss

© 2017

Fahima Fahmida Islam

All Rights Reserved

ABSTRACT

Among the different probes to study the structures of the bio and structural materials, X-ray and neutron are widely used because of their distinctive usefulness in investigating different structures. X-ray radiography and neutron diffraction are two widely known non-destructive techniques for material inspection. Here we demonstrate the design of neutron diffractometer with low power source and analyze the digital image produced by the X-ray radiography instead of neutron diffraction because of the availability of the data. Neutron diffraction is a powerful tool for understanding the behavior of crystal structures and phase behaviors of materials. While neutron diffraction capabilities continue to explore new frontiers of materials science, such capabilities currently exist in limited places, which require high neutron flux. The study seeks to design a low-resolution neutron diffraction system that can be installed on low power reactors (e.g. 250 kW thermal power). The performance of the diffractometer is estimated using Monte-Carlo ray-tracing simulations with McStas with an application in material science. Both monochromatic and polychromatic configurations are considered in order to maximize the net diffracted neutron flux at the detectors with reasonable resolution. On the other hand, considering X-ray radiography as a structure inspecting technique, analysis of dental X-ray panorama is performed for the detection of oral lesions. A novel automatic computer-aided method to identify dental lesions from dental X-ray is presented. Morphological operations, intensity profile analysis, automated seed point selection, region growing, feature extraction and neural network application are carried out to perform the job. Results show that the performance of the proposed method surpasses existing automated methods utilizing dental X-rays.

ACKNOWLEDGMENTS

I am especially grateful to Dr. Hyoung Koo Lee for giving me the opportunity to pursue research providing with scientific guidance, constant support and sharing his knowledge relating to image reconstruction.

I would also like to thank Muhammad Abir for sharing his vast knowledge on image processing and Matlab. I also thank Dr. Xin Liu and Dr. Ayodeji Alajoa for being a member of my thesis defense.

Finally, I would like to acknowledge my family members: my father, Muhammad Nazrul Islam, my mother Mahmuda Islam, my sister Sanzida Islam, my brother in law Muhammad Azam have supported me in every moment.

TABLE OF CONTENTS

	Page
ABSTRACT	iii
ACKNOWLEDGMENTS	iv
LIST OF ILLUSTRATIONS	viii
LIST OF TABLES	x
SECTION	
1. INTRODUCTION	1
1.1. MOTIVATION	1
1.1.1. The Role of X-ray and Neutron.....	1
1.1.2. Digital Image Produced by Radiography and Diffraction.....	2
1.1.3. The Same Application Field for Neutron and X-ray	6
1.2. THE GOAL AND LAYOUT OF THE WORK	7
2. NEUTRON POWDER DIFFRACTION.....	9
2.1. PHYSICAL CONCEPT OF NEUTRON POWDER DIFFRACTION	9
2.1.1. Scattering Cross-section	9
2.1.2. Neutron as a Wave	11
2.1.3. Why Diffraction Occured	13
2.1.4. Derivation of Bragg's Law	16
2.1.5. Bragg's Equation in Reciprocal Lattice	17
2.1.6. Powder Diffraction	24
2.1.7. Bragg Peak and Indexing	26
2.1.8. Performance Metrics	26
2.2. INSTRUMENTATION	28
2.2.1. Neutron Source.....	28
2.2.2. Monochromator/Analyzer	29
2.2.3. Soller Collimator	32
2.2.4. Detectors.....	32
2.2.5. Samples and Environment.....	33
2.3. DESCRIPTION OF THE ACTUAL WORK	35

2.3.1. Current Status	35
2.3.2. Description of the Beamline	36
2.3.3. Monochromator Configuration.....	39
2.3.4. Polychromatic Configuration	41
2.4. RESULTS	43
3. AUTOMATIC DETECTION OF CARRIES FROM DENTAL X-RAY	48
3.1. BACKGROUND FOR CARRIES DETECTION	48
3.1.1. Dental Carries and Dental Cancer	48
3.1.2. Common Methods to Analyze Dental Carries	48
3.1.3. Application of Panorama Dental X-ray in Detection Carries.....	48
3.1.4. Computet Aided Detection	49
3.1.5. Characteristics of the Carries	49
3.2. IMAGE PROCESSING AND DETECTION METHODS.....	50
3.2.1. Average Intensity Projection	50
3.2.2. Otsu's Thresholding.....	50
3.2.3. Gaussian Smoothing Filter	51
3.2.4. Sobel Edge Detector	52
3.2.5. Erosion Operation.....	52
3.2.6. Row by Row Labelling of Connected Components.....	53
3.2.7. Region Growing	54
3.2.8. Feature Extraction	55
3.2.9. Hough Line Transform.....	55
3.2.10. Artificial Neural Network	56
3.3. DESCRIPTION OF THE ACTUAL WORK	57
3.3.1. Current Status	57
3.3.2. Data-set.....	58
3.3.3. Periodontium Identification	58
3.3.4. Sructure Detection	64
3.3.5. Cystic Features Extraction.....	65
3.4. RESULTS	67

3.5. DISCUSSION AND CONCLUSION 69
BIBLIOGRAPHY 71
VITA 78

LIST OF ILLUSTRATIONS

Figure	Page
1.1. Comparison of cross sections for X-ray and neutron for certain elements.....	2
1.2. Length and time scales available to X-ray radiography and neutron diffraction.....	3
1.3. DEI-CT slice image from an intact cadaveric right knee joint.....	4
1.4. The experimental setup for DEI acquisition.....	6
2.1. The geometry used for the definition of scattering cross-section.....	10
2.2. Neutron acting as a wave.....	12
2.3. Bragg's law description.....	15
2.4. Bragg's law derivation.....	17
2.5. Two dimensional monoclinic lattice and its reciprocal space.....	18
2.6. In case of elastic scattering the wave and its nature.....	20
2.7. Geometrical representation of the crystal atomic lattice plane with respect to the real space basisvectors.....	22
2.8. The neutron spectra at the entrance of the beam tubes at FRM II.....	25
2.9. Monochromator take-off angle of 120 at HRPT.....	25
2.10. Comparison of different diffractometer resolutions.....	27
2.11. The rocking curve for Ge monochromator at HB-2a.....	29
2.12. Vertically focusing Ge wafer monochromator at HRPT.....	30
2.13. The neutron detector array at NPDF,NCSU.....	33
2.14. The NRS beam line.....	39
2.15. The monochromatic layout of NRS beamline.....	39
2.16. Gauge volume.....	42
2.17. The schematic rotation set up for polychromatic configuration.....	42
2.18. The polychromatic layout of NRS beamline.....	43
2.19. The comparison of the diffracted intensity between NRS and D1B.....	43
2.20. The shifting of the peaks by changing the wavelengths.....	44
2.21. The scattered peaks for the variation of wavelengths.....	45
2.22 The resolution function of wavelengths.....	45
2.23. The scattered peaks for the variation of scattering angles.....	46

2.24. The resolution function of scattering angles.....	47
3.1. Gaussian filter.....	51
3.2. Erosion method.....	53
3.3. Connected components.....	54
3.4. Steps of the region growing algorithm.....	54
3.5. The representation of a line.....	55
3.6. Landmarks of panoramic X-rays.....	59
3.7. Hard palate detection.....	61
3.8. Preliminary ROI detection.....	62
3.9. An OPG ROI and the average intensity profiles.....	63
3.10. Refined ROI detection.....	64
3.11. Connected component division.....	64
3.12. Region growing methods.....	65
3.13. The regions that define the ratios RU and RO.....	67
3.14. Cross mark of the cyst.....	67
3.15. The feedforward neural network architecture.....	68
3.16. The validation performance curve.....	69

LIST OF TABLES

Table	Page
2.1. Coherent scattering cross-sections for X-ray and neutron.....	9
2.2. Selection of wavelength for Ni.....	28
2.3. The measurement of neutron flux at sample position at the existing instruments at some neutron beam laboratories.....	34
2.4. Aperture diameter and corresponding L/D ratio.....	37
2.5. Collimator step diameters.....	37
2.6. Beam transit tube step diameters.....	38
2.7. Bragg's peaks for different analyzer takeoff angles.....	44
2.8. Bragg's peaks for different scattering angles.....	46
3.1. Otsu's thresholding method calculation.....	51
3.2. Performance criteria.....	69

1. INTRODUCTION

1.1. MOTIVATION

In this section the motivation of the work will be described. This section will also highlight the relation of the different sections of the work.

1.1.1. The Role of X-ray and Neutron. The knowledge of the structure of materials and medical science is critical to detect flaws, pores, voids, and other imperfection in the materials. Among the various probes to study the structure of the material, X-ray and neutron are widely used because of their distinctive usefulness in investigating different structures. They are complementary to one another in providing information about the material. To understand which one is suitable for what kind of materials to be investigated, it is worthwhile to compare their total cross sections as shown in Figure 1.1. It is important to note that, compared to neutron cross sections (blue and green circles), the X-ray cross sections (red circle) are considerably larger, which signifies that for equivalent incident flux and sample size, an X-ray probing technique would produce a stronger signal. Since for X-rays, the cross section is related to the number of electrons, they increase consistently with the gradual increment of the atomic number in the periodic table. Because of this property, hydrogen positions in the heavy elements (e.g., metal ions) would be difficult to determine when being examined with X-ray. Furthermore, a feeble distinction between adjacent elements, as can be depicted for the transition metals Mn, Fe and Ni in Figure 1.1, would make it difficult to identify them from their compounds. These issues could be resolved with neutron when used as a probe because of the dependence on its total cross sections on the details of the nuclear structure and thus produce a non-order relationship with an atomic number of the elements in the periodic table. As an example, a very high contrast in the total cross section exists between Mn and Fe for the neutron, as shown in Figure 1.1. With neutrons, not only is the hydrogen atom clearly visible when being present with such heavy elements like uranium, but also the isotopes of the hydrogen H and D can be clearly identified. To investigate individual molecules in a soft condensed matter, this information is very valuable.

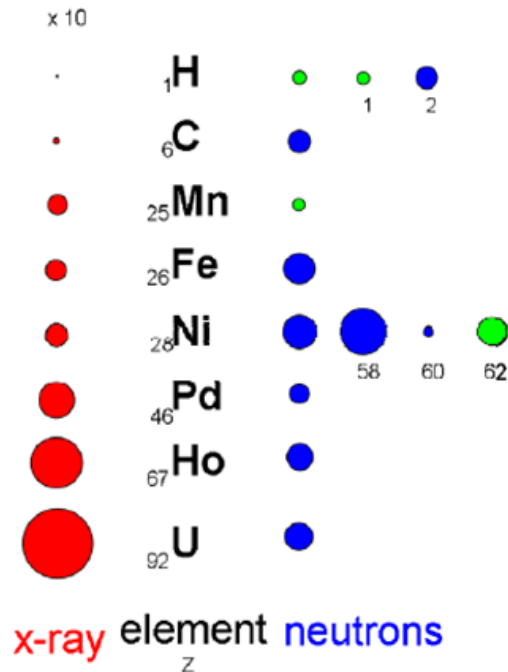


Figure 1.1. Comparison of cross sections for X-ray and neutron for certain elements [1].

1.1.2. Digital Image Produced by Radiography and Diffraction. X-ray radiography and neutron diffraction are two widely known non-destructive techniques for material inspection. While radiography is typically used as a 2D imaging mechanism for the information about the outer structural composition or integrity, diffraction is usually used to reveal the atomic structure of the crystal object as a diffraction pattern. Due to the different natures of the interactions among the different probes and the target materials, in most of the cases, different techniques that are used to examine the structure of the material provide information that is complementary to one another, as shown in Figure 1.2.

Radiography is produced because of the absorption property of the radiation, while diffraction occurs due to the scattering property. However, results of both techniques could be treated as a digital image. The image is called radiography because of absorption, while the image produced because of the diffraction is called diffraction enhanced imaging. The difference between absorption and diffraction-enhanced imaging (DEI) can

be explained with a drop of water. Instead of absorbing the X-ray or neutron waves or particles, water diffracts and bends them in different directions. Zhong and his team[1] thought the same theory could work for medical diffraction technology.

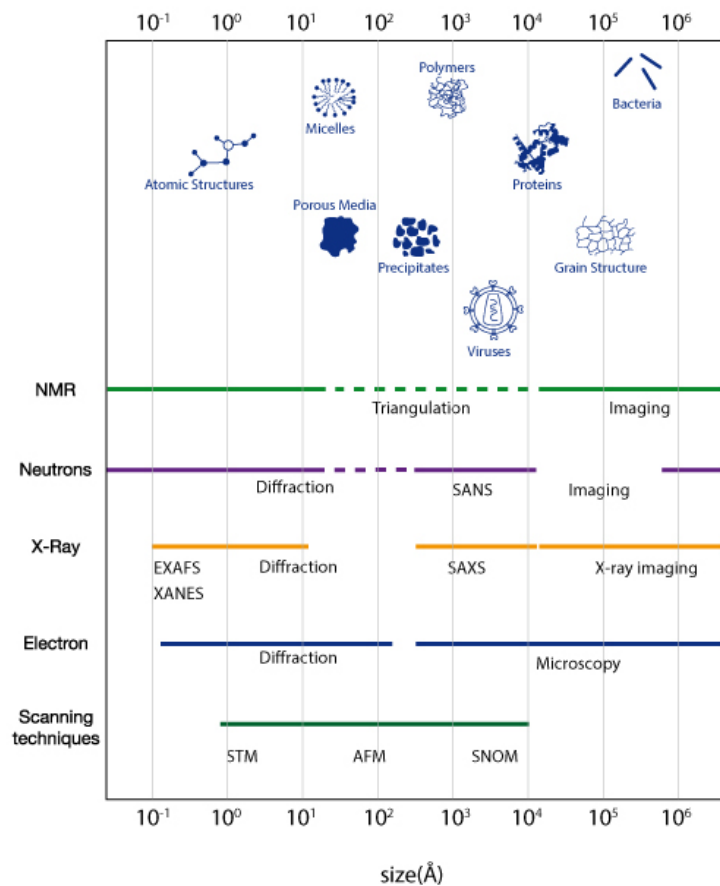


Figure 1.2. Length and time scales available to X-ray radiography and neutron diffraction [2].

With DEI, the wave is diffracted as it travels through the region of the body being imaged. Because of not being absorbed, the extent of radiation left in the human body is comparatively less than that of conventional radiography. This fact captures the attention of the radiology community to use DEI as a potential two-dimensional imaging mechanism for finding details such as liquid in muscles and tendons [shown in Figure 1.3] and lesions in breast tissue.



Figure 1.3. DEI-CT slice image from an intact cadaveric right knee joint.

Since the radiation dose required for DEI is comparatively so small in amount (for reference, it equals only 1% of conventional radiography), it is also far less costly than conventional imaging techniques such as MRI, CT, or ultrasound. Though DEI produces images similar to MRI, images created with DEI have a better resolution through the use of a probe with a short wavelength such as neutron or X-ray. Because of its superior quality and low dose, it could replace conventional radiography in the near future.

The application of DEI in the medical section would cover the patient across all ages for different diagnostic purposes. Because of its low dose, it would be very useful for the diagnosis of children. There have been numerous studies done on the usefulness of DEI to breast and other imaging methods. Radiography produces shades of gray for the different parts of the body based on the different amounts of radiation being absorbed. Because of the different radiation absorbing power of different parts of the human body based on their thickness, some thicker parts give a clear image where the soft part like soft tissue, tumor, or cyst are difficult to image because they are not thick enough to absorb the radiation. To apprehend distinct differences between a cyst and its neighboring normal tissues with radiation, a higher dosage of radiation is needed. This is a very critical concern regarding breast imaging, which leads to an alternative that uses a lower dosage. From the research conducted through the last ten years on DEI, it can be said that DEI could be considered as a safe, efficient imaging alternative.

A study conducted by Pisano and Zhong [3] in 2000 showed that DEI can produce enhanced visibility of speculated surface of breast cancer specimens similar to biopsy in six out of seven cases compared to digital radiographs. Researchers also found that enhanced contrast is achieved by DEI because of its refractive properties, which make the

early detection of breast cancer possible with the help of digital mammography detectors. In 2003, another study was done on the soft tissue in the foot and ankle with DEI and radiography and found that DEI contributes to higher-contrast imaging of noncalcified soft tissues such as muscles, tendons, adipose tissue, and cartilage. The result of this study makes DEI more suitable for soft tissue imaging than conventional radiography.

The process employed for DEI is similar to the typical diffraction experiment. Conventionally, a brighter, more intense beam is used as a source. A monochromatic beam with a single wavelength from the source is chosen for imaging. When a single wavelength is chosen, the flux will automatically be reduced. Therefore, it would be necessary to test if low power source would be able to make a diffraction experiment. With the collaboration of Brookhaven National Laboratory and the University of North Carolina (UNC) School of Medicine, a 2D DEI machine is currently under development.

The principle of DEI is laid on how the radiation passing through the body bends and scatters. These properties change in a very delicate way among various sorts of tissue. Three causes of imaging contrast, scatter, refraction and absorption, are the key features that are used by the DEI to deliver the information on the diffraction of the wave passing through the different tissues. To examine the matter with DEI, a silicon crystal is used between the target and the image detector as shown in Figure 1.4. Diffraction and scattering of different amounts of radiation occur based on the different composition of the tissues once the radiation strikes the target. After passing through the sample, the radiation hits the crystal and is diffracted again by different amounts. The silicon crystal acts as an analyzer and makes DEI distinctive by transforming the imperceptible variations in scattering angles generated by the different tissues into intensity variation that can be easily identified by a typical radiation detector. The output is exceptionally detailed images that are unique to different kinds of soft tissue such as cysts and tendons. The conventional relationship between the wavelength of the radiation and the target material described by Bragg's law must be satisfied. Monochromator is required to produce monochromatic radiation required for diffraction. Zhong and his group [1] used the radiation source with analyzer shown in Figure 1.4 for the diffraction experiment to be used as imaging modalities for medical imaging purposes.

1.1.3. The Same Application Field of Neutron and X-ray. Although X-ray medical imaging is a widely performed diagnostic procedure in medicine, neutron could also be potentially used. Neutron imaging experiments using the High Flux Isotope Reactor (HFIR) are performed to image healthy and cancerous breast tissue samples. In order to prevent the development of the cancer, the transformation of the tumor should be detected at an early stage with adequate information, which would be possible with the help of hydrogen-sensitive neutron imaging. Neutrons are considered an *in vitro* effective complementary imaging system for biopsied tissues of several centimeters thick because they prevalently recognize hydrogen in the tissue, which is one of the most plenteous components in nature. The imaging with neutrons could make advance detection possible not only for breast cancer but also for other varieties of cancers.

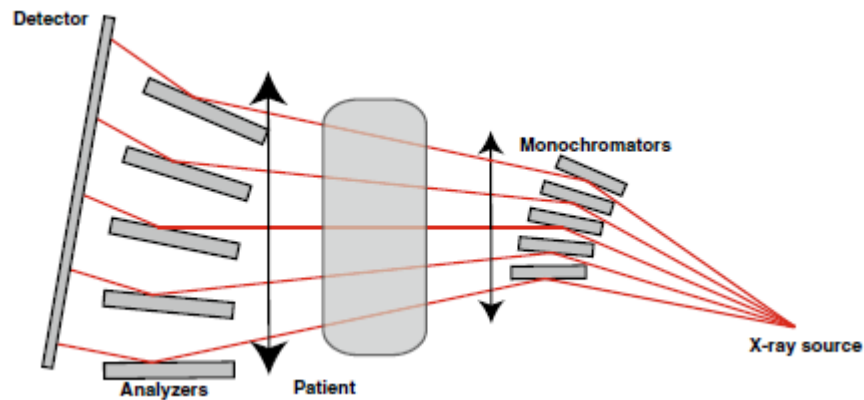


Figure 1.4. The experimental setup for DEI acquisition

Though until now all of the clinical studies with neutron imaging mentioned below were performed for *in vitro* conditions, *in vivo* neutron imaging capabilities for clinical application is under investigation [4,5]. Previous works showed that a distinction among the trace element concentrations associated with cancer has been found *in vitro* for various kind of cancers of the breast [6,7,8,9,10], colon [11, 12, 13,14, 15,16,17, 18], lung [9], prostate [19, 20,21, 22, 23, 24,25, 26,27, 28, 29], kidney [11], liver [11, 29, 26, 27, 28] stomach [11], urinary bladder [11], testis, and female reproductive organs [11].

Besides the clinical section, the application of X-ray and neutron imaging to inspect the non-clinical industrial materials is very well known and well established. For example neutron DEI plays an important role in studying crystallography and phase composition of nuclear fuel material. Because of the different crystal structure and different crystal properties, fuel materials show different crystallographic change during heating and irradiation. Changing of the thermal properties of the material also change the crystallographic phase of the material. These changes should be investigated for the proper performance of nuclear fuel. Neutron DEI is a great tool to serve this purpose.

1.2. THE GOAL AND LAYOUT OF THE WORK

Since both the x-ray radiography and neutron diffraction are used for diagnosis purpose and they could produce the digital image, if we could analyze the digital image produced by either, it is possible to analyze the digital image produced by another one. The challenge of using the DEI is the capability of low power source to make the system work. Here we demonstrate the design of neutron diffractometer with low power source and analyze the digital image produced by the X-ray radiography instead of neutron diffraction because of the availability of the data. X-ray radiography of dental image is considered is one of the most complicated images to analyze. If it is possible to analyze the dental X-ray radiography successfully, it is believed that any kind of digital image could be analyzed in a similar way. The results of low power neutron diffractometer simulation and computer aided analysis of X-ray radiography support the concept of computerized analysis of neutron diffraction induced digital image produced by low power source.

The work is divided into two main parts. Part 1 will present the design of neutron diffractometer with low power reactor, particularly using the neutron radiography reactor (NRAD) at Idaho National laboratory (INL). Part 2 will describe the computer aided automatic analysis of the dental x-ray radiography in order to find out the lesions. Each part will be divided into subsections. The first subsection will present the physical concepts underlying the proposed methodology described to accomplish the goal. The second subsection will described the novel methodology that is developed to acquire the

goal. The third subsection will present the results of the methods described. Finally, the fourth subsection will conclude the challenges to be overcome along with the potential application.

2. NEUTRON POWDER DIFFRACTION

2.1. PHYSICAL CONCEPT OF NEUTRON POWDER DIFFRACTION

In this section the physical concept behind the neutron diffraction phenomenon is described. The principles of diffraction, the Braggs Law, the nature of neutron are described in this section.

2.1.1. Scattering Cross-section. Diffraction is an elastic scattering. The elastic scattering happens when the energy or wavelength of the particles or the waves remains unchanged after getting scattered. Scattering cross section of the elements is the parameter that causes the scattering events as tabulated in Table 2.1. [1].

Table 2.1. Coherent scattering cross-sections for X-ray and neutron

Elements	Coherent Scattering X-secs for X-rays [barn]	Coherent Scattering Cross sections for Neutrons
${}^1\text{H}$	0.66	1.76
${}^6\text{C}$	24	5.55
${}^{25}\text{Mn}$	416	1.75
${}^{26}\text{Fe}$	450	11.22
${}^{28}\text{Ni}$	522	13.30
${}^{46}\text{Pd}$	1408	4.39
${}^{67}\text{Ho}$	2986	8.06
${}^{92}\text{U}$	5631	8.90

The scattering cross section can be defined using the Figure 2.1. In this figure, if j particles per area and time, defined by the incident beam flux, hit the object in the \underline{k} direction and get scattered with n particles per second under the scattering angle of 2θ in

the \underline{k}' direction and are seen by a detector with the solid angle of $d\Omega$, then the angular dependent differential elastic scattering cross section is defined by

$$\frac{d\sigma}{d\Omega} = \frac{n}{jd\Omega} \quad (1)$$

The integration of Equation 1 over the angular range from 0 to 4π gives the angular independent total scattering cross section, which is expressed by the following equation.

$$\sigma = \int_0^{4\pi} \frac{d\sigma}{d\Omega} d\Omega \quad (2)$$

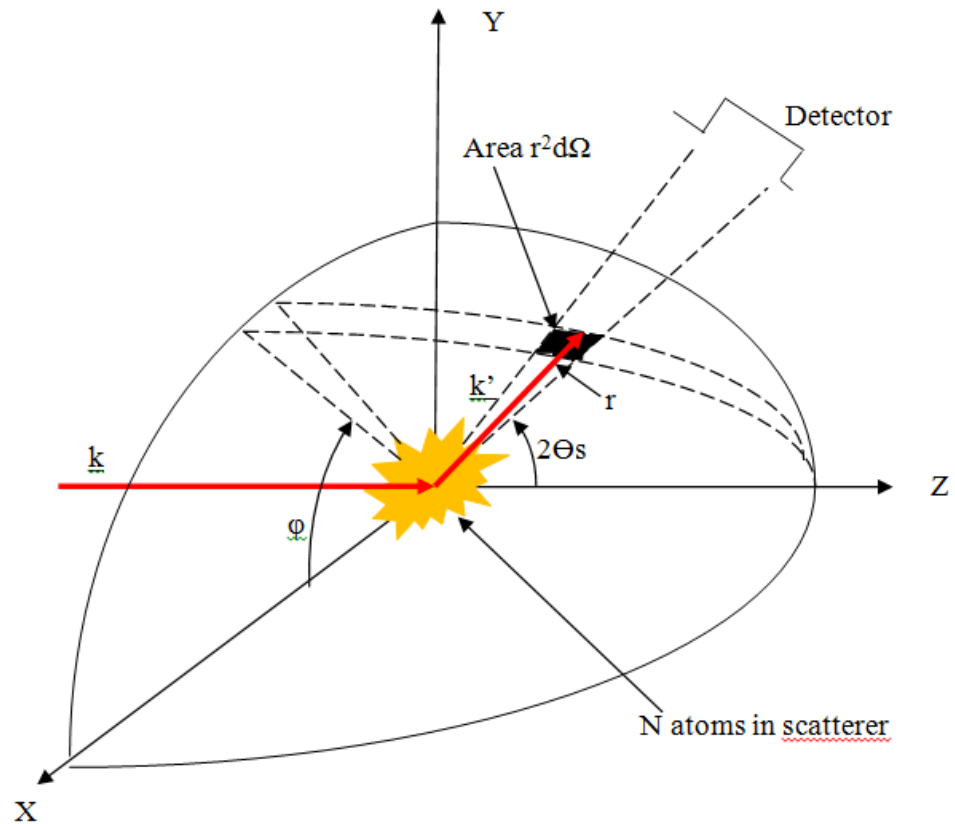


Figure 2.1. The geometry used for the definition of scattering cross-section.

In the scattering event, another important parameter is the scattering vector, \underline{Q} , which is defined by the difference of the incident wave vector (\underline{k}) and the scattered wave vector (\underline{k}') of plane waves with the wavelength of λ .

$$\underline{Q} = \underline{k}' - \underline{k} \quad (3)$$

$$\underline{k} = \hat{k} \cdot \frac{2\pi}{\lambda} \quad (4)$$

$$\underline{k}' = \hat{k}' \cdot \frac{2\pi}{\lambda} \quad (5)$$

The magnitude of the scattering vector could be represented in terms of λ and Θ by the following:

$$Q = |\underline{Q}| = \sqrt{(\underline{k}' - \underline{k})^2} = \sqrt{k^2 + k'^2 - 2k \cdot k'} = \sqrt{k^2 + k'^2 - 2kk' \cos 2\theta}$$

(6)

$$\Rightarrow Q = \sqrt{k^2 \frac{4\pi^2}{\lambda^2} + k'^2 \frac{4\pi^2}{\lambda^2} - 2k \frac{2\pi}{\lambda} k' \frac{2\pi}{\lambda} \cos 2\theta} = \sqrt{\frac{4\pi^2}{\lambda^2} (k^2 + k'^2 - 2kk' \cos 2\theta)}$$

(7)

$$\Rightarrow Q = \sqrt{\frac{4\pi^2}{\lambda^2} (1^2 + 1^2 - 2 \cos 2\theta)} = \sqrt{\frac{4\pi^2}{\lambda^2} 2(1 - \cos 2\theta)} = \sqrt{\frac{4\pi^2}{\lambda^2} 2(2 \sin^2 \theta)}$$

...(8)

$$\Rightarrow Q = \frac{4\pi}{\lambda} \sin \theta \quad (9)$$

2.1.2. Neutron as a Wave. The neutron scattering phenomena, as shown in Figure 2.2, is considered as quantum mechanical process where, formally described by the wave nature of neutron and the nucleus of the matter. The wave nature of neutron is helpful to explain the likelihood of locating a position of neutron in space along with the particle image of neutron. The neutron incident on the nucleus of the target at a fixed time can be represented by a wave having the amplitude of unity with the wave function:

$$e^{i\vec{k}\cdot\vec{r}} \quad (10)$$

The probability of finding the neutron in any position of \vec{r} is the same because the squared modulus value of the wave function is one for all of the positions of \vec{r} .

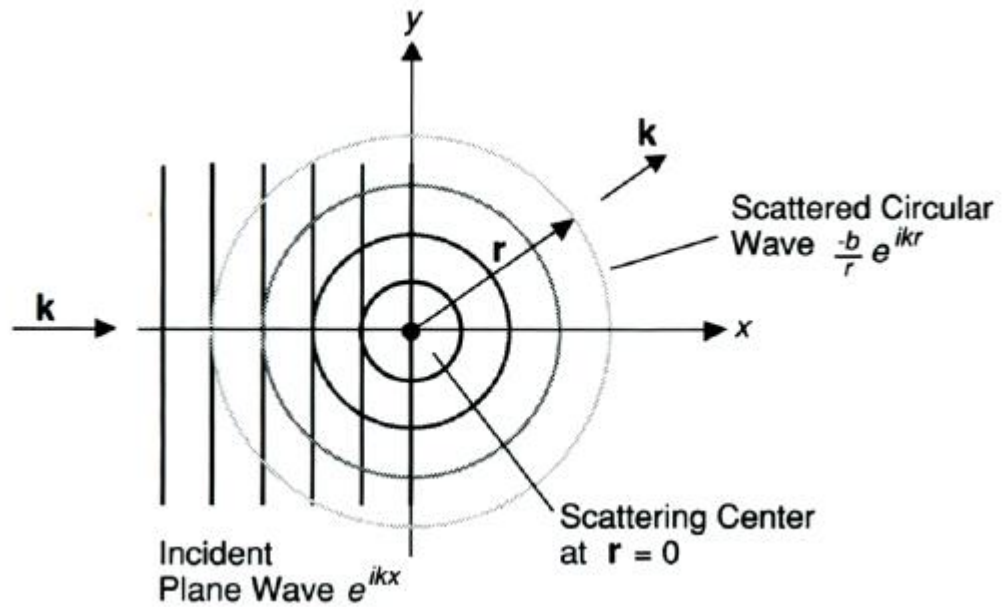


Figure 2.2. Neutron acting as a wave: A neutron beam hitting on a solitary dispersing focus and going in the horizontal direction can be characterized by a plane wave $e^{i\vec{k}\cdot\vec{r}}$ with the amplitude of unity. Since the neutron sees the dissipating focus (a core) as a point, the scattering will be isotropic. Therefore, the scattered neutron shaft spreads out in round wavefronts (here drawn as circles) with the amplitude of b/r . The $1/r$ part of this representation, when squared to get neutron intensity, represents the $1/r^2$ diminish in power with a separation that happens as the scattered wavefront develops in size. Since we have taken the diffusing focus to be inflexibly settled, the scattering is elastic—that is, there is no adjustment in the neutron's energy—so the episode and scattered wavevectors both have same value for k [30].

For a neutron, travelling as a wave with a fixed value of momentum, $mv = h\nu/2\pi$, in the \vec{k} direction parallel to the x- direction, the nodes of the wave function are shown in Figure 2.2 as straight wave fronts. The stronger the interaction between the neutron and the nucleus of the target, the higher the value of the amplitude of the scattered wave. Due

to the isotropic property of the scattered wave, the wave function can be expressed as $(-b/r)e^{i\vec{k}\cdot\vec{r}}$ when the location of the nucleus of the target material is considered as at the origin of the coordinate system.

The circles in fig diffusing out from the target are used to represent the scattered spherical wavefronts. The term $1/r$ in the scattered wavefunction maintaining the inverse square law states that the neutron intensity, given by the square of the wavefunction, decreases as the inverse square of the distance from the scattering nucleus. The symbol “ b ” in the wavefunction of the scattered neutron represents the scattering length of the target material which is a constant parameter. The scattering length is used to estimate the strength of the interaction between the neutron and the target materials. Because of the repulsive interaction between neutron and the target, the negative sign in front of “ b ” is used to preserve the positive value of ‘ b ’. The scattering phenomenon is considered as elastic because there is no change in the neutron’s energy and the internal state of the nucleus remains the same due to the collision between them. The wave vector k remains unchanged before and after the collision in the elastic scattering.

2.1.3. Why Diffraction Occurred. Diffraction is a type of coherent scattering. When the neutron wave incident on each atom, the atom will act as a center of the spherical scattered wave which has a specific phase compared to other waves that are scattered. After being scattered from the array of crystal, in the particular direction, the waves will reinforce each other. There is a close relationship between these directions and the inter-atomic spacing of the crystal array.

In order to find out the symmetrical property and the lattice dimension of a crystal, the direction where the constructive interference happened is used. Although diffraction is considered an elastic scattering process, according to Van Hove formula, the diffracted intensity is calculated by integrating the following equation over the energy E .

$$V(\vec{r}) = \frac{2\pi\hbar^2}{m} \sum_j b_j \delta(\vec{r} - \vec{r}_j) \quad (11)$$

where, $V(\vec{r})$ represents the potentiality of the neutron wave being scattered. Here m denotes the neutron mass and $\delta(\vec{r})$, named as Dirac delta function, is used to gives the

value of one when the position within \vec{r} and otherwise zero. ‘ b_j ’ represents the scattering length described above and \hbar is Plank’s constant. The integral of the above equation over E provides another Dirac delta function $\delta(t)$ which implies that the pair correlation between r and t must be evaluated at $t=0$. The result of the integration could be represented by the following equation for a sample with only one isotope:

$$I(\vec{Q}) = b_{coh}^2 \sum_{i,j} \langle e^{i\vec{Q} \cdot (\vec{r}_i - \vec{r}_j)} \rangle \quad (12)$$

The locations of the nuclei represented by i and j must be examined at the same time. For the static atoms in the crystal, \vec{r}_i and \vec{r}_j are constant and the thermodynamic averaging brackets can be disregarded from the above equation. In real life, the crystal atoms continuously move back and forth about their steady state position and stay only a very small amount of time in the equilibrium position. This fact presents another factor with the thermodynamic averaging and makes the above equation as:

$$I(\vec{Q}) = b_{coh}^2 \sum_{i,j} e^{i\vec{Q} \cdot (\vec{r}_i - \vec{r}_j)} e^{-Q^2 \langle u^2 \rangle / 2} = \left| b_{coh} \sum_i e^{i\vec{Q} \cdot \vec{r}_i} \right|^2 e^{-Q^2 \langle u^2 \rangle / 2} \equiv S(\vec{Q}) \quad (13)$$

The factor $e^{-Q^2 \langle u^2 \rangle / 2}$ is known as Debye-Waller factor and $\langle u^2 \rangle$ represents the mean value of the squared amount of displacement of the atoms from their steady state position. The above equation gives the scattered intensity of the neutrons denoted by $S(\vec{Q})$ which is called the structure factor. Since, a crystal is made of so many atoms and each of them has the influence on phase factor of the above equation, the value of $S(\vec{Q})$ is always any value other than zero for any value of Q . The Figure 2.3 could be used to deduce the values of Q which provides the non-zero values of $S(\vec{Q})$.

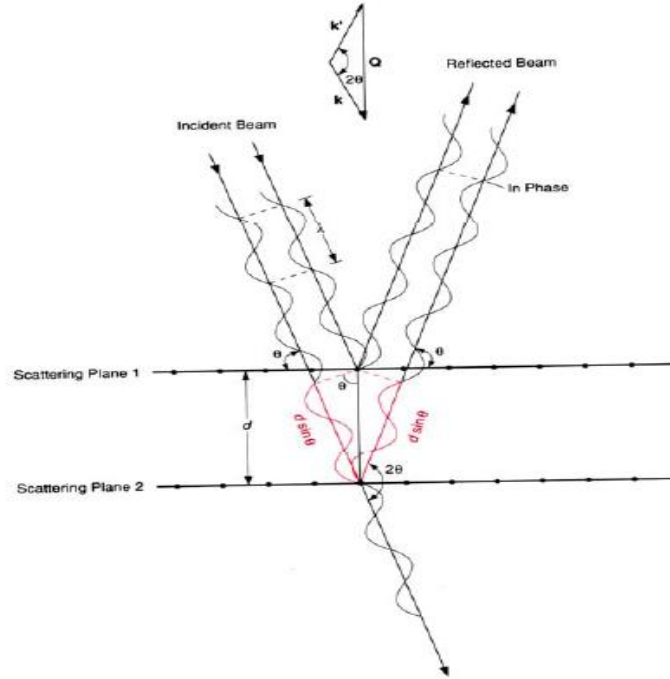


Figure 2.3. Bragg's law description: constructive impedance happens when the waves scattered from adjoining diffusing planes of atoms stay in phase. This happens when the distinction in distance traveled by waves scattered from adjoining planes is a whole number of wavelength. The figure demonstrates the additional path traveled by the wave scattered from Scattering Plane 2 will be $2 d \sin \theta$. At the point when that path length difference is set equivalent to $n\lambda$ (where n is a number), the outcome is Bragg's Law $n\lambda = 2 d \sin \theta$. Primary scattering happens when $n = 1$, however, higher-order Bragg scattering is also viewed for different estimations of n [30].

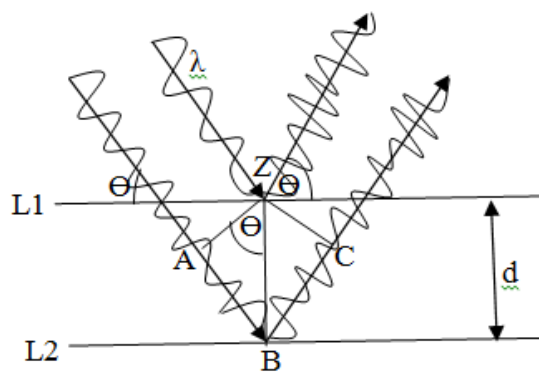
In the Figure 2.3, Q is the perpendicular plane to the atomic plane where scattering occurs (e.g. scattering plane 1 and 2). Q is represented as the integral multiple of $2\pi/d$ where d is the interplanar atomic distance. This representation leads the value of $\vec{Q} \cdot (\vec{r}_i - \vec{r}_j)$ as a multiple of 2π and keeps the value of each exponential factor in the summation operation in the above equation as one. This phenomenon makes the value of $S(\vec{Q})$ non-zero. Here, for the diffraction to happen, the direction of \vec{Q} has to be perpendicular to the direction of the planes of atoms. The relationship among λ , θ and d provides the condition for diffraction discovered by William Bragg known as Bragg's law:

$$n\lambda = 2d \sin \theta \quad (14)$$

When the incident wavelength λ and the scattering angle θ satisfy the above equation, diffraction would occur from any of the planes of the atoms. In real experiment the crystal is rotated unless the correct orientation for diffraction is obtained when Q is perpendicular to the plane responsible for scattering and a signal appears in the detector. This signal is called the Bragg peak. The equation providing the scattered neutron intensity implies that the intensity after scattering is proportional to the squared value of the atomic density of the scattering plans. Hence analysis of the scattered intensity peaks will help to determine not only the inter-planar spacing, but also the density of the atoms. For getting the diffracted peak in the detector, the sample has to be rotated for a specific incident wavelength in order to satisfy Bragg's law.

2.1.4. Derivation of Bragg's Law. A simple geometry can be used to derive Bragg's law. The difference between the distances travelled by two neutron waves scattered from two consecutive atomic planes is considered to derive from Bragg's law. In Figure 2.4, L1 and L2 are two consecutive atomic planes with their spacing of d . If two neutron waves hit them, AB and BC represent the extra distance travelled by the neutron wave hitting the lower plane. According to the Bragg's law, in order to have constructive interference or to have the same phase for both of the scattered waves, the extra distances (AB+BC) must be an whole number (n) multiple of the wavelength (λ). Thus:

$$n\lambda = AB + BC \quad (15)$$



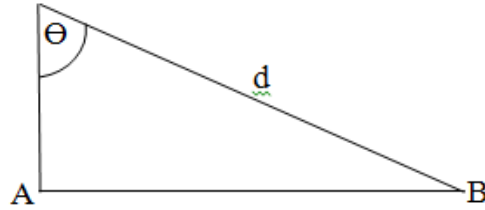


Figure 2.4. Bragg's law derivation

As shown in Figure 2.4, as the triangles ABZ and ZBC are identical, $AB=BC$, Equation 1 can be written as the following:

$$n\lambda = 2AB \quad (16)$$

As d is the hypotenuse of triangle ABZ, shown in the Figure 2.4, AB can be written as the following equation in terms of inter planar spacing d and the incident angle θ :

$$AB = d\sin\theta \quad (17)$$

From equation 16 and 17, $n\lambda$ can be expressed as

$$n\lambda = 2d\sin\theta \quad (18)$$

Equation 18 is known as Bragg's law.

2.1.5. The Bragg's Equation in Reciprocal Lattice. Reciprocal lattice is an imaginary lattice introduced by the crystallographer in order to understand the diffraction phenomena by a crystal in a more convenient way. A reciprocal lattice could be imagined as a lattice having the lattice parameters of a^* , b^* , c^* , α^* , β^* and γ^* with the volume of V^* which are related to the normal crystal lattice having the lattice parameters of a , b , c , α , β and γ and the volume of V by the following equations:

$$a \cdot b^* = a \cdot c^* = b \cdot c^* = a^* \cdot b = a^* \cdot c = b^* \cdot c = 0 \quad (19)$$

$$a \cdot a^* = b \cdot b^* = c \cdot c^* = 1 \quad (20)$$

The so called reciprocal points in the reciprocal lattice situated in the reciprocal space are related to the Miller indices used to define the atomic planes. For each atomic plane, one point is assigned in the reciprocal lattice. If h_{hkl} represents the vector from the origin to any point (hkl) in the reciprocal space, then

$$h_{hkl} = ha^* + kb^* + lc^*; \quad h, k, l \in Z \quad (21)$$

where,

$$a^* = x(b \times c) \quad (22)$$

where x is the scale factor and can be derived as:

$$a^* \cdot a = x(b \times ca) = xV \Rightarrow x = \frac{1}{V} \quad (23)$$

Figure 2.5 shows the 2D reciprocal lattice with the corresponding real lattice for the monoclinic structure.

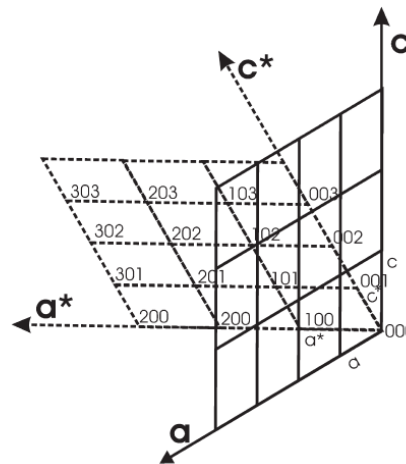


Figure 2.5. Two dimensional monoclinic lattice and its reciprocal space[31]

From the value of x , the following can be written:

$$a^* = \frac{1}{V}(b \times c), \quad b^* = \frac{1}{V}(c \times a), \quad c^* = \frac{1}{V}(a \times b), \quad (24)$$

and the other way around:

$$a = \frac{1}{V^*}(b^* \times c^*), \quad b = \frac{1}{V^*}(c^* \times a^*), \quad c = \frac{1}{V^*}(a^* \times b^*) \quad (25)$$

The following equations are used to describe the relationship between the real lattice parameters and the reciprocal lattice parameters:

$$a^* = \frac{bc \sin \alpha}{V}, \quad (26)$$

$$b^* = \frac{ac \sin \beta}{V}, \quad (27)$$

$$c^* = \frac{ab \sin \gamma}{V}, \quad (28)$$

$$\cos \alpha^* = \frac{\cos \beta \cos \gamma - \cos \alpha}{\sin \beta \sin \gamma}, \quad (29)$$

$$\cos \beta^* = \frac{\cos \beta \cos \gamma - \cos \alpha}{\sin \beta \sin \gamma}, \quad (30)$$

$$V = abc \sqrt{1 + 2 \cos \alpha \cos \beta \cos \gamma - \cos^2 \alpha - \cos^2 \beta - \cos^2 \gamma} \quad (31)$$

It is important to reproduce Bragg's law with vectors shown in Figure 2.6. In the above figure, s_0 and s represents the incident and scattered wave vectors respectively.

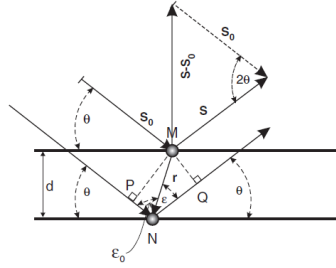


Figure 2.6. In case of elastic scattering the wave and its nature [31]

Their magnitude is the same as the wavelength λ as it is considered as elastic scattering and their direction is in the direction of the incident wave and the direction of the scattered waves respectively. The scattering vector can be written as:

$$h = (s - s_0) \quad (32)$$

The length of h can be given by the following equation whereas its direction is in the perpendicular direction to the scattering plane.

$$\frac{h}{s} = 2 \sin \theta \quad (33)$$

The comparison of the above equation, the Bragg's equation can be written as:

$$\frac{n\lambda}{d} = 2 \sin \theta \quad (34)$$

which provides:

$$\frac{n\lambda}{d} = \frac{h}{s} \quad (35)$$

Assigning the magnitude of s to $\frac{1}{\lambda}$, Bragg's equation can be obtained in terms of the magnitude of the scattering vector h :

$$h = \frac{n}{d} \quad (36)$$

The above equation shows the condition of the diffraction phenomena in terms of the reciprocal lattice space. The conditions say that in order to have diffraction occur, the scattering vector h must be an integral of the reciprocal lattice spacing $1/d$. If d^* represents the vector perpendicular to the lattice planes with the magnitude of $1/d$, the scattering vector \mathbf{h} can be represented as:

$$h = nd^* \quad (37)$$

Different orders n of diffraction can occur for the same atomic plane with different scattering angles 2θ . In the following equation n is used to list the lattice planes:

$$d_{nh,nk,nl}^* = nd_{hkl}^* \quad (38)$$

From the above equation, it can be understood that $d_{222}^* = 2d_{111}^*$ which provides another representation of Bragg's equation as follows:

$$h = d_{hkl}^* \quad (39)$$

The relationships of the real space basis vectors and d_{hkl}^* are depicted in Figure 2.7.

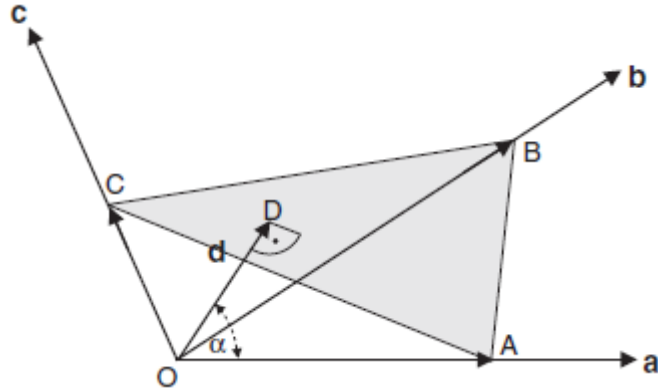


Figure 2.7. Geometrical representation of the crystal atomic lattice plane with respect to the real space basis vectors [31]

Using Figure 2.7, d_{hkl}^* can be defined using the real space basis vectors a , b and c .

$$OA = \frac{1}{h}a, \quad OB = \frac{1}{k}b, \quad OC = \frac{1}{l}c \quad (40)$$

where, h , k and l are the three integers known as Miller indices that are used to uniquely define the set of parallel planes appearing periodically in the lattice. The vector d_{hkl} perpendicular to scattering plane initiates from one plane and end on the next parallel scattering plane. Thus, $OA \cdot d = (OA)d \cos \alpha$. From the geometry of the Figure 2.7, it can be written that $(OA) \cos \alpha = d$. By replacing, it is obtained that, $OA \cdot d = d^2$. Using this information, the above equation can be written as:

$$\frac{1}{h}a \cdot d = d^2 \quad (41)$$

and similarly,

$$h = a \cdot \frac{d}{d^2}, \quad k = b \cdot \frac{d}{d^2}, \quad l = c \cdot \frac{d}{d^2} \quad (42)$$

According to the definition, h , k and l are Miller indices where they are divided by their largest common integers. Therefore, d_{hkl}^* can be written in terms of vector d :

$$d_{hkl}^* = \frac{d}{d^2} \quad (43)$$

which provides

$$d_{hkl}^* = ha + kb + lc \quad (44)$$

Additionally, d_{hkl}^* can be expressed in terms of the reciprocal lattice basis by the following equation:

$$d_{hkl}^* = ha^* + kb^* + lc^* \quad (45)$$

which was deduced utilizing

$$d_{hkl}^* \cdot a^* = ha \cdot a^* + kb \cdot a^* + lc \cdot a^* = h \quad (46)$$

$$d_{hkl}^* \cdot b^* = ha \cdot b^* + kb \cdot b^* + lc \cdot b^* = k \quad (47)$$

$$d_{hkl}^* \cdot c^* = ha \cdot c^* + kb \cdot c^* + lc \cdot c^* = l \quad (48)$$

The comparison between the equations $d_{hkl}^* = ha^* + kb^* + lc^*$ and $h_{hkl} = ha^* + kb^* + lc^*$ verifies the character of d_{hkl}^* and the reciprocal space lattice vector h_{hkl} . Hence, Bragg's equation can be rewritten as

$$h = h_{hkl} \quad (49)$$

In terms of the reciprocal lattice vector, it can be said that diffraction happens when the scattering vector h and the reciprocal lattice vector h_{hkl} are equal. This concept is used to construct an Ewald sphere.

In terms of reciprocal lattice vector, Braggs's equation can be written as

$$|h| = |s - s_0| = \frac{2 \sin \theta}{\lambda} = \frac{1}{d} \quad (50)$$

2.1.6. Powder Diffraction. In contrast to single crystal diffraction, powder diffraction offers a huge practical advantage of obtaining the chemical compounds much more easily in the form of a powder or polycrystalline bulk sample rather than in the form of a single crystal. Powder sample has randomly-oriented crystallites (powder grains) which causes an overlapping of diffraction signals from different lattice planes with the same interatomic spacing. This phenomenon reduces the number of independent observables, however makes the data collection process significantly faster and simpler. Therefore powder diffraction studies are typically used for the examination of the structural or magnetic subsystem of polycrystalline materials under the influence of external parameters (temperature, pressure, magnetic field, mechanical force, electric field etc.) by monitoring their evolution “live”[2]. These features, along with the fact that the both quantitative and qualitative approach could be used to perform compositional sample proof (phase analysis), make the powder diffraction especially powerful in the characterization of new materials. Research areas typically include materials for post irradiated nuclear fuel, lithium-ion batteries, ionic conductors of different kinds, ferroelectrics and multiferroics, hydrogen storage materials, engineering alloys, superconductors and strongly correlated electron systems, minerals and geological samples [2].

There are two neutron powder diffraction method: reactor (continuous wavelength) is used as the neutron source. Some important features of this type of method are described. Continuous neutron flux is produced. Figure 2.8 shows [2] the neutron spectra at the entrance of the beam tubes at 20 MW reactor power at FRM II.

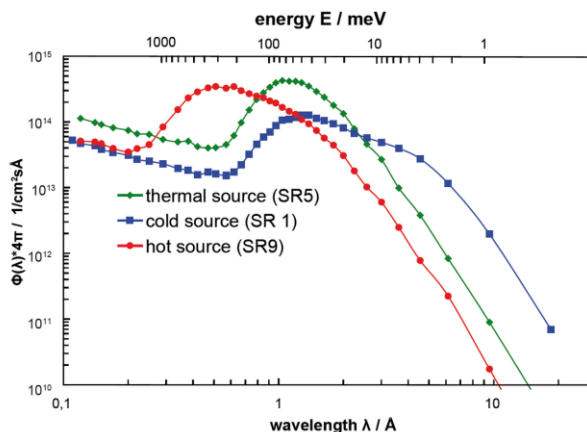


Figure 2.8. The neutron spectra at the entrance of the beam tubes at FRM II [2]

Single wavelength is selected using monochromator. Position sensitive detectors are used which record neutron rate as a function of diffraction angle. Bragg's law ($\lambda = 2d \sin\theta$) is obeyed. Resolution and intensity are controlled primarily by appropriate primary/secondary collimations and take-off-angle of the monochromator. Generally, The resolution ($\Delta d/d$) depends on: monochromator, monochromator take-off angle, monochromator mosaicity and take-off angle. Figure 2.9 [32] shows the monochromator take-off angle.

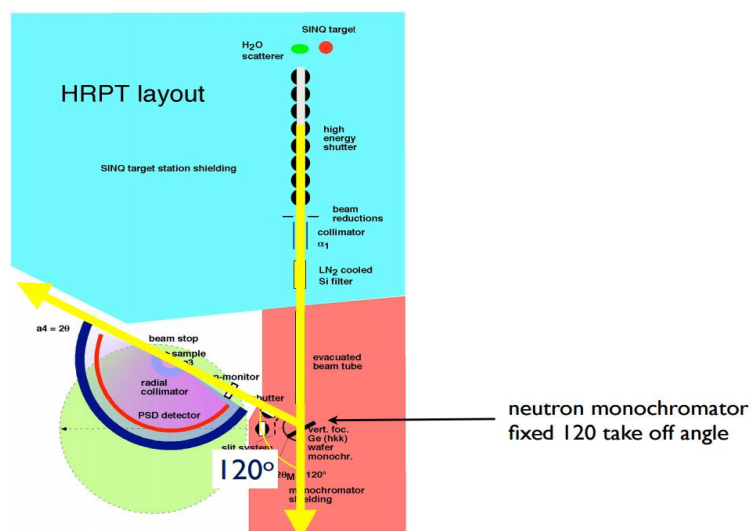


Figure 2.9. Monochromator take-off angle of 120 at HRPT [32]

Some of the examples of this type are: C2 Chalk River, Canada; HB-2A HFIR, Oak Ridge; SPODI, FRM II, DE. Another method is Time of Flight Method (for Spallation Sources of neutrons). Here choppers close to the target (6m and 9m) are used to select neutron pulses for example: HRPD (ISIS, U.K.)

2.1.7. Bragg Peak and Indexing. For complicated structures, it is difficult for indexing accurately from the Bragg scattering profile. Because of the less symmetry and more unit cell volumes of the complex structure, the position of the Bragg's peaks are overlapped with each other, hence are difficult to find out. The inter planar spacing d_{hkl} is a function of the miller indices as well as the unit cell dimensions. The d-spacing can be found out from the Bragg's peak position, θ obtained in the diffraction experiment. The Bragg peaks should be indexed with miller indices. The determination of miller indices from d-spacing is depending on the shape and dimensions of the unit cells. Large takeoff angle of monochromator increase the resolution at the cost of the reduction of the neutron flux. On the other hand, large mosaicity increases the neutron flux while making the resolution comparatively poor.

2.1.8. Performance Metrics. The optimization between the neutron flux at the sample and the resolution of the detected peak governs the performance of a low power neutron diffractometer.

The expected resolution can be calculated for a fixed wavelength (λ) with a fixed scattering angle. From the relationship [33] between the scattering vector (Q) and the scattering angle (θ_s), the resolution $\Delta Q/Q$ can be calculated by assuming that λ and θ_s are independent to each other when act as contributors to resolution calculation:

$$\Delta Q/Q = \{(\Delta\lambda/\lambda)^2 + [\Delta\theta_s \cot(\theta_s)]^2\}^{1/2} \quad (51)$$

where

$$\Delta\lambda/\lambda = \Delta\theta_a \cot(\theta_a) \quad (52)$$

$$\Delta(2\theta_a) = 2\Delta(\theta_a) = \gamma/(\alpha_2^2 + \alpha_3^2 + 4\eta^2)^{1/2} \quad (53)$$

$$\gamma^2 = 4[\alpha_2^2\alpha_3^2 + \alpha_2^2\eta^2 + \alpha_3^2\eta^2] - 4a\alpha_2^2(\alpha_3^2 + 2\eta^2) + a^2[\alpha_1^2\alpha_2^2 + \alpha_2^2\alpha_3^2 + \alpha_1^2\alpha_3^2 + 4\eta^2(\alpha_1^2 + \alpha_2^2)]$$

$$(54)$$

$$a = (d\lambda / d\theta)_s / (d\lambda / d\theta)_a = [d_{hkl} \cos(\theta_s)] / [d_{PG} \cos(\theta_a)] \quad (55)$$

where, $\Delta\theta_s$ is considered as the sample-detector collimation and θ_a is the analyzer takeoff angle and calculated from the Bragg's equation:

$$\theta_a = \sin^{-1}(\lambda / 2d_a) \quad (56)$$

where, d_a is the analyzer lattice spacing. η is the analyzer mosaicity and $\alpha_1, \alpha_2, \alpha_3$ are the collimation for source-sample, sample-analyzer and analyzer-detector respectively. In Figure 2.10, a comparison of a diffractometer [34] of three different resolution (D1B- low resolution diffractometer (PG monochromator, large $\Delta\lambda/\lambda$); D1A- medium resolution diffractometer (Ge monochromator, narrow $\Delta\lambda/\lambda$); D2B- high resolution diffractometer (Ge Monochromator, narrow $\Delta\lambda/\lambda$)) are illustrated. It is shown that for low resolution diffractometer, the optimum resolution is achieved for a lower range of scattering angles compared to higher order resolution diffractometer.

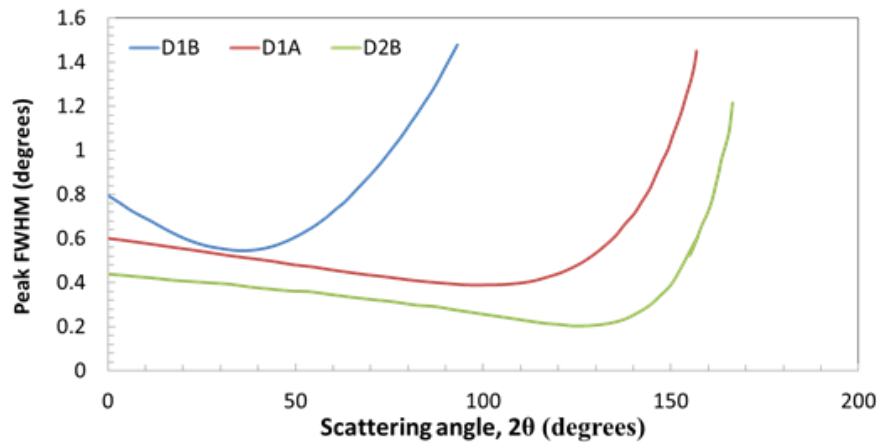


Figure 2.10. Comparison of different diffractometer resolutions[34]

2.2. INSTRUMENTATION

In this section the instrumentation of diffractometer is described. A short description of neutron source, monochromator, collimator, detector and sample are given in this section.

2.2.1. Neutron Source. Thermal Neutron distribution with its velocity(v) or energy ($E = \frac{1}{2}mv^2$) follows the Maxwellian distribution for a particular moderator temperature T , which can be expressed with the following equation:

$$\phi = v^3 e^{(-mv^2/2K_B T)} \quad (57)$$

The important criteria to select the wavelength are given below:

- The selected wavelength should give more than 10 scattered peaks with reasonable magnitude in order to have the structure solution.
- For the purpose of structure refinement, more than 10 peaks should be achieved with the selected wavelength.
- In a special sample environment which limits the range of diffraction peaks, shorter wavelength is recommended to use.

A shorter wavelength is preferable in order to have sufficient peaks needed for the specific purpose as shown in Table 2.2.

Table 2.2. Selection of wavelength for Ni

12		d (Å)	2.0345	1.762	1.246	1.063	1.02	0.881	0.81	0.788	0.7	0.678	0.7	0.62	0.6
Ni		λ (Å)	111	200	220	311	222	400	331	420	422	431	210	521	440
	36	1.5	43.264	50.39	74.02	89.8	95	116.7	136	144.3	###	#####	###	####	###
	32	1.6	46.31	54.01	79.9	97.69	104	130.5	163	#####	###	#####	###	####	###
	28	1.7	49.391	57.69	86.04	106.3	113	149.6	#####	#####	###	#####	###	####	###
	25	1.8	52.51	61.44	92.5	115.8	124	#####	#####	#####	###	#####	###	####	###
	23	1.9	55.672	65.26	99.37	126.8	138	#####	#####	#####	###	#####	###	####	###
	20	2	58.881	69.16	106.8	140.5	159	#####	#####	#####	###	#####	###	####	###
	19	2.1	62.142	73.16	114.9	162.4	#####	#####	#####	#####	###	#####	###	####	###
	17	2.2	65.459	77.27	124	#####	#####	#####	#####	#####	###	#####	###	####	###
	15	2.3	68.839	81.49	134.7	#####	#####	#####	#####	#####	###	#####	###	####	###
	14	2.4	72.289	85.86	148.8	#####	#####	#####	#####	#####	###	#####	###	####	###
	13	2.5	75.817	90.38	#####	#####	#####	#####	#####	#####	###	#####	###	####	###

2.2.2. Monochromator/Analyzer. A monochromator is a (number of) single crystals that is used to monochromate or select the neutron wavelength according to Bragg's law. The range of wavelengths accepted depends on the mosaicity of the crystal which can be described as a measure of the spread of the orientation of the crystal plane. Empirically rocking curve is determined to measure the mosaicity. Figure 2.11 shows the rocking curve for Ge monochromator at HB-2a at Oak Ridge national Laboratory [35]. Though a larger mosaicity increases the number of neutrons that will make it to the sample, reduces the energy resolution[36].

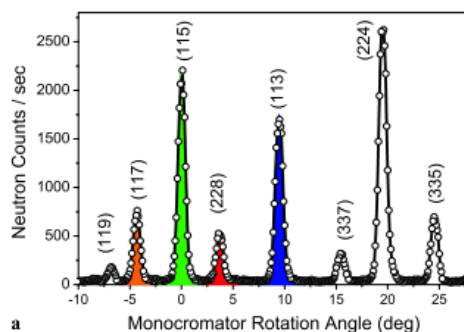


Figure 2.11. The rocking curve for Ge monochromator at HB-2a[35]

The materials that are commonly used as monochromator crystals are Pyrolytic Graphite, Silicon, Copper, Beryllium, and Heusler crystals. The choice of monochromator depends on the range of incident wavelength required for the experiment, and the desired energy resolution. The added advantage of the silicon (111) reflection is that the second order ($n=2$) neutrons are forbidden (and most neutrons seem to know this) [36].

Focused monochromators can be used as a way to increase the neutron flux. The collection of small crystals that are used to make monochromators can be lined up in such a way that the beam will be focused in the horizontal or vertical plane (or both). Focusing in the vertical plane is like a simple concave mirror whereas focusing in the horizontal plane is by diffraction - i.e. the beam from the sample is focused on the detector [37]. This way can produce more scattering events by focusing a neutron beam that is larger

than the sample onto the sample, though this comes at the cost of reduced resolution. However, for a large range of experiments, a decoupled treatment can be considered by maintaining the resolution in the horizontal plane and relaxing the resolution in the vertical plane, thereby greatly increasing the number of neutrons detected. In fact, the resolution in the vertical plane tends to be compromised from the outset, leading to the shape of most neutron detectors[36]. Figure 2.12 shows the vertically focusing Ge wafer monochromator at HRPT.



Figure 2.12. Vertically focusing Ge wafer monochromator at HRPT[32] .

The monochromator, along with the detector, is one of the most essential elements in order to decide the neutron intensity other than the size of the sample. Since the intensity is directly proportional to the band of wavelength, the band of wavelength $\Delta\lambda/\lambda$ which is as wide as possible is desirable. A wider wavelength band can be obtained by employing a larger value of mosaic spread $\Delta\theta_M$ for the monochromator, since again differentiating Bragg's equation $2d\sin\theta_M=\lambda$ for scattering from the monochromator provides:

$$\Delta\lambda/\lambda = \Delta\theta_M \cot(\theta_M) \quad (58)$$

Since this equation for $\Delta\lambda/\lambda$ is similar to the equation achieved by differentiating Bragg's equation $2d\sin\theta=\lambda$ for scattering from the sample: $\Delta d/d = \Delta\theta \cdot \cot \theta$, it would seem as if the large $\Delta\lambda/\lambda$ and high intensity indicate large peak widths $\Delta d/d$. Luckily, this is not the case. After diffracting from the monochromator, the different wavelengths in different directions are fetched to the same direction when diffracted by the sample for the second time. This is only true for the circumstances when the scattering angle caused by the sample 2θ is equal to the monochromator 'take-off' angle $2\theta_M$, and is called 'reciprocal space' or wavelength focusing.

A small take-off angle θ_M for the increased value of $\cot \theta_M$ would also increase $\Delta\lambda/\lambda$ and hence, increase the intensity. However, having the smaller value of take-off angle would focus the wavelength to small scattering angles. In practice, since, focusing at large angles is desirable, a larger monochromator mosaic is used to compensate. A monochromator mosaic of 15 minutes is not too much for even the highest resolution neutron powder diffractometer. Considering that a 30 minute wide collimator should be used in order to allow the entire wavelength band to reach the sample. Practically, no collimator is used at all; therefore, the determination of α_3 is made by the size of the sample divided by the distance to the collimator.

In order to increase the intensity vertical divergence of the incident beam can also be considered since it does not affect much the instrumental resolution. The value of vertical divergence can be used as much as 5 degrees on a diffractometer by which a comparatively high resolution in the equatorial plane could be still maintained. Vertical divergence is achieved by insertion the diffractometer configuration as near as possible to the source, and having a large aperture in the reactor. However, when this condition does not produce sufficient intensity, a vertically focusing monochromator must be used.

Vertical focussing is accomplished by cutting the monochromator horizontally into strips, and adjusting the strips on a vertically bended support plate to center onto the sample. For example, on D2B at ILL Grenoble, 30 x 1cm strips are used to focus a 4cm high sample by a neutron beam of 30 cm width. The focal length can be remained constant for different wavelengths by fixing the monochromator take-off angle as large as possible[38].

For low flux reactor highly oriented pyrolytic graphite is a good choice to be used as a monochromator for various reasons. Since it offers large mosaic spread it keeps the flux as maximum as possible compared to the other materials used as monochromator. Since, neutrons do not absorb large wavelength, and hence the peak to background ratio is improved because of the direct proportional relationship of the detected intensity and the wavelength, 002 graphite plane could be used as monochromator which provides the wavelength of 2.4 Å for the low takeoff angle of 42°. If a graphite filter is used between the monochromator and the sample, $\lambda/2$ harmonic contamination can be avoided.

2.2.3. Soller Collimator. Collimators are used to define the direction of travel of the neutron. It can be said that the better defined the beam, that is, the narrower the distributions, the more accurate the measurement, that is, the higher the resolution and the larger the coherence volume. Normally Soller collimators are used for diffraction purpose. It could be long thin parallel sheets of neutron absorbing coated, separated by an appropriate distance to provide the desired beam divergence[35].

Soller collimators α_1 assist to shape the course of the beam hit to the monochromator. They comprise of a layer of uniform absorbing plates. The divergence is controlled by the proportion of the separation length between the plates. Therefore, their length is dissociated from the beam cross section, which is deduced from the cross section of the layer. In the comparison with a perfect collimator, neutron loss can be determined from the the ratio of the plate width to the distance between the plates.

The utilization of a very thin extended plastic foils as the plates makes a major progress in neutron collimation.. For instance, if the foils with the thickness of 25 μ with a coating of another neutron absorber (gadolinium oxide paint) of 25 μ thickness is used 90% productivity can be achieved regardless the possibility that the plate spacing is just 0.5mm which is normally maintained for a 5 minute collimator with the length of 34cm . The collimator of such kind provides the beam with the cross section of 25x100 mm or more. While the width beam controls the sample width, the height of the beam is crucial for acquiring higher vertical divergence for the intensity increment. [39].

2.2.4. Detectors. In case of reactor neutron source, monochromatic neutron beam is scattered by the sample and recorded in the position sensitive detector (PSD). The detector records the count as a function of the scattering angle. Normally ^3He tubes with

Soller collimators are used for detector. ^3He detectors are most useful for the suppression of gamma background, and usually has the most homogenous distribution of detector efficiency for the individual channels. In this sense, the data corrections after acquisition need minimal effort and the collected scattering data are most reliable. Each detector channel of Silicon-based detectors with extremely high counting rates (many MHz) and spatial resolution (55 μm) produced by the Dutch company Amsterdam Scientific Instruments is equipped with individual electronics, which serves these high demands. For counting neutrons, there should be a boron-based converter. Gamma sensitivity is the drawback of this technique, and such events must be suppressed by software. The practical signal to noise ratio must be explored experimentally. However, this technique is suitable for the central ‘beam-stop’ detector, which determines the wavelength dependent transmission and center position.

The range of the scattering angle determines the rotational angular range of the detector. The diffraction patterns recorded by detector consist of a series of peaks as a function of scattering angle. Rietveld analysis techniques is used to analyze the diffraction patterns in which the position of the peak is related to the diffraction from atomic planes with different inter planar spacing. Figure 2.13 [37] shows the neutron detector array at NPDF, NCSU.

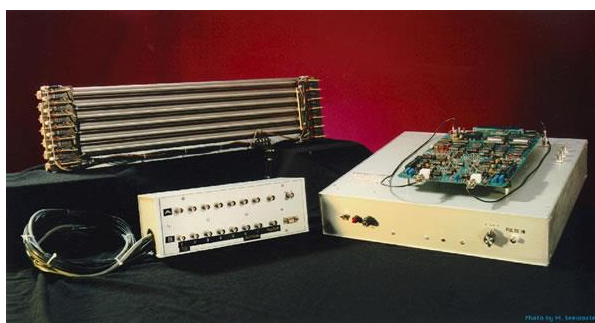


Figure 2.13. The neutron detector array at NPDF, NCSU[37]

2.2.5. Samples and Environment. For powder diffraction, the sample is usually used in a tube shape. The advantage of this kind of shape is the sample can be sealed

easily. Usually goniometer is used to precisely control the physical location and orientation of the sample. The sample is generally placed at the centered of the beam using precise control of the horizontal motions of the sample goniometer, with a neutron camera that is positioned in the path of the neutron beam behind the sample[35]. Various environments such as high temperature, low temperature, high magnetic field, and high pressure could be created in which the sample can be placed.

The measurement of neutron flux at the sample position is crucial to know for the diffraction experiment. Table 2.3 provides the measurement of neutron flux at sample position at the existing instruments at some neutron beam laboratories[37].

Table 2.3. The measurement of neutron flux at sample position at the existing instruments at some neutron beam laboratories[37]

Diffraction Facility	Power (MW)	Source Flux (n/cm²/s)	Sample Volume	Sample Flux (n/cm²/s)
NIST BT-1 Cu-311/15'	20	$4 \cdot 10^{14}$	10 cm ³	$4 \cdot 10^5$
NIST BT-1 Cu-311/7'	20	$6 \cdot 10^{14}$	10 cm ³	$2 \cdot 10^5$
MURR PSD-II	10	$6 \cdot 10^{13}$	0.35 cm ³ to 1 cm ³	$1.35 \cdot 10^5$
NCSU NPDF	1	$2.7 \cdot 10^{12}$	0.35 cm ³ to 1cm ³	$0.64 \cdot 10^5$
HB2-HFIR	85			$\sim 10^7$

2.3. DESCRIPTION OF THE ACTUAL WORK

The description of the methodology developed is provided in this section. Before the description some literature is also reviewed here.

2.3.1. Current Status. Idaho National Laboratories (INL) intends to leverage its expertise in both x-ray diffraction and neutron radiography to facilitate a new neutron diffraction diagnostic at the Hot Fuel Examination Facility (HFEF). Neutrons for the diagnostic will be produced by the Neutron Radiography reactor (NRAD), a 250 kW TRIGA (Training, Research, Isotopes, General Atomics) reactor. Two beam lines extend from the NRAD: the North Radiography Station (NRS) to the north and the East Radiography Station (ERS) to the east. Each beamline exits into a shielded chamber designed to house experimental radiography specimens. The ERS is currently dedicated to neutron radiography[40], but the NRS is not actively used. This work evaluates the feasibility of operating a neutron diffractometer at the NRS in its current state and proposes modifications to the beamline with conventional instrumentation of diffractometer. The modifications optimize the diffractometer's performance by increasing the intensity of the neutron beam reaching the sample, without sufficient neutron intensity, the diffractometer may not produce the desired results due to noise. The performance of the proposed instrumentation is compared with D1B diffractometer at ILL. A new polychromatic design, with wider range of wavelengths, for environments that preclude cumbersome rotation of the sample is also proposed and computationally evaluated.

This study concentrates exclusively on powder samples which are more representative of specimens studied at the HFEF and are more readily available than single crystal samples. Both the monochromatic and polychromatic wavelength dispersive techniques are explored for powder diffraction.

Direct modeling of neutron beams plays an essential part in planning new capabilities and upgrading existing instrumentation for neutron diffraction. As such, the current NRS beamline geometry is modeled and a diffractometer using a monochromator is evaluated using the Monte Carlo code McStas. The diffractometer performance with and without the proposed modifications to the NRS beamline are compared. Additionally, polychromatic wavelength dispersive diffraction is evaluated for the modified NRS

beamline. Based on the results of these simulations, recommendations for further development of the beamline are made.

Recently, McStas has become pervasive in diffractometer simulation literature. Cussen, et al. used McStas to compare different diffractometer instrument configurations. They compared experimental results two instruments, a collimated high resolution constant wavelength powder diffractometer and a conventional open geometry constant wavelength powder diffractometer, to McStas simulation and were able to propose an improved configuration. They also cross checked the McStas results with the Vitess code and found the results to be consistent with each other [41]. Willendrup et al. modeled the DMC powder diffractometer at the Paul Scherrer Institute using McStas and found good agreement in peak positions, peak widths, background intensity and relative peak intensities between the experimental and simulated setups [42]. Nagler et. al designed and simulated the CG1 beamline at HFIR (High Flux Isotope Reactor) with McStas. They conducted analytical calculations and Monte Carlo calculations using both McStas and IDEAS. The two codes were in agreement [43]. Artus et. al designed the new thermal single crystal diffractometer at FRM-II. Although they carried out the simulation for the optimization of all the optical components regarding the intensity, divergence, peak profiles and wavelength resolution, they presented their work for neutron guide [44].

Mathematical approaches for beamline optimization are now available in for constant wavelength powder diffractometer. However, Monte Carlo simulations typically require fewer mathematical assumptions and those assumptions are also found in the purely mathematical treatments, such as assuming the monochromator being treated as though it were infinitely thin [41]. Fewer assumptions makes Monte Carlo simulation more reliable in most circumstances.

2.3.2. Description of the Beamline. The NRS beamline begins 60 cm from the NRAD reactor core as a rectangular channel where neutrons exit the reactor. An aperture assembly system is installed next to the exit point to control the L/D ratio, where L is the distance from the aperture to the sample and D is the diameter of the aperture. Two interchangeable aperture blocks provide three L/D ratios. One block has a single 8.9 cm diameter aperture. The other has two apertures whose selection is controlled by sliding the

block vertically. The apertures dimensions are tabulated in Table 2.4 [40]. Both aperture blocks are made of combat grade boron nitride with a tapered circular opening.

Table 2.4. Aperture diameter and corresponding L/D ratio

Aperture diameter (cm)	L/D ratio
2.3	700
5.3	300
8.9	185

From the aperture, the beam passes through a removable stepped aluminum collimator inserted into a steel-lined penetration (60 cm diameter) in the concrete shielding and north reactor room wall. The collimator provides four diverging steps with diameters given in Table 2.5. Each step of the collimator consists of a 25.4 cm thick boron carbide annulus. The entire collimator is 173 cm long.

Table 2.5. Collimator step diameters

Step Number	Diameter (cm)
1	10.4
2	11.7
3	13.3
4	14.9

Neutrons passing through the collimator enter a containment box including a gamma shield, a neutron shutter and a shaper. The neutron shaper changes the beam cross section to a rectangle sized typical radiography foil.

Following the containment box is an 1176 cm beam transit tube comprised of nineteen diverging steps. The steps allow the beam to diverge; the diameter of each step is

given in Table 2.6. The transit tube lining is composed of boral, cadmium, lead and indium.

Table 2.6. Beam transit tube step diameters

Step Number	Diameter (cm)
1	18.8
2	20.6
3	21.9
4	24.2
5	26.0
6	27.8
7	29.6
8	31.4
9	33.0
10	35.0
11	36.8
12	38.6
13	39.1
14	42.1
15	43.9
16	45.7
17	47.5
18	49.4
19	51.1

A beam scraper made of cadmium, boral and masonite with variable heights and widths is placed just before the specimen holder. The scraper can extend to 0.432 cm in height and 0.355 cm in width to accommodate different sample sizes. The specimen holder is approximately 200 cm from the exit of the beam transit tube and can support

cylindrical samples up to 0.25 cm diameter and 4 cm height. Most of the beamline is filled with a helium atmosphere to minimize scatter. The thermal neutron flux is approximately 1.4×10^{12} n/cm²-s at the aperture with a moderator temperature of 300 K [45]. Figure 2.14 shows the layout of NRS beam line.

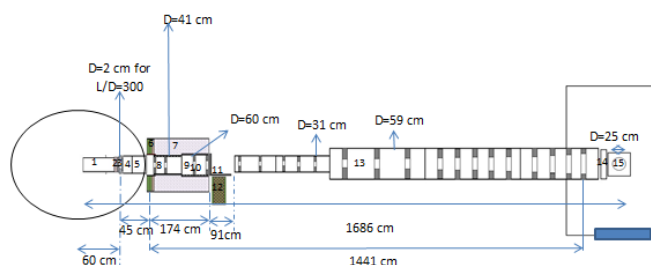


Figure 2.14. The NRS beam line: (1) rectangular channel; (2) filter block; (3) aperture assembly; (4) short tube; (5) long tube; (6) borated polyethylene and polyethylene disc; (7) lead shield; (8) through wall collimator I; (9) through wall collimator II; (10) collimator insert; (11) neutron shutter; (12) gamma shutter; (13) beam transit tube; (14) scraper assembly; (15) specimen holder. Figure is not shown to scale.

2.3.3. Monochromator Configuration. The current NRS configuration modeled in McStas is shown in Figure 2.15. The source was modeled as a disk located at the beam aperture emitting particles uniformly into a cone of 2.5° . Simulations were run using 10^6 neutron rays; each simulation required approximately 30 minutes on an Intel® Xeon® CPU E5-2603 @ 1.80 GHz.

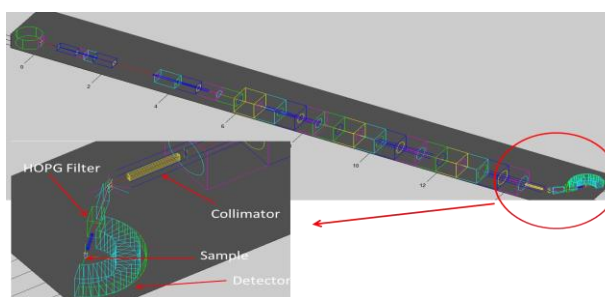


Figure 2.15. The monochromatic layout of NRS beamline.

A simple simulation was run in McStas with only the beam transit tube modeled to determine the intensity incident on the monochromator location. The maximum intensity of 1.0×10^5 n/s-Å was found at 1.18 Å.

A Highly oriented pyrolytic graphite (HOPG)-002 crystal (oriented such that the angle of incidence between the plane defined by the 002 Miller Indices and the primary beam is θ_m), was selected for the monochromator and placed after the beam transit tube 14.41 m from the source. This monochromator has an intrinsic d -spacing, d_m , of 3.354 Å. The simulated crystal was curved with a horizontal and vertical mosaicity of 12 minutes to focus the monochromatized beam onto the sample.

The 1.54 Å wavelength was selected as the monochromatized wavelength. Although the effect of the wavelength on the optimization is not as clear from the simulations, the wavelength should be selected such that it can measure the desired ranges of d -spacings[46]. Using Bragg's Law, the scatter angle off the monochromator, $2\theta_m$, was computed to be 25.84°.

A cylindrical nickel powder sample was modeled 10 cm from the monochromator. The sample was 4 cm tall with a radius of 0.25 cm. In reality, a single detector would measure the intensity as the sample is rotated by a goniometer. However, modeling transient motion within a Monte Carlo simulation is onerous so instead, the sample remains stationary and a banana detector is used to measure the angular intensity distribution. Angular data points are converted to d -spacing using Bragg's Equation. The computed d -spacing values are compared to a reference data set obtained from the experimental result from D1B, ILL for $\text{Na}_2\text{Ca}_3\text{Al}_2\text{F}_{14}$ power samples.

Three collimators, one between the source and monochromator, one between the monochromator and sample, and one between the sample and detector, were added. The beam quality was also enhanced by shaping the beam holes, including collimator divergence.

A Söller blade linear collimator is inserted into the beam tube. The collimator has a horizontal divergence of 18 minutes and is placed 15 m downline from the source. Past the collimator, a slit is used to absorb any neutrons not headed directly toward the monochromator. The slit is assumed to be very thin and completely absorbing. The monochromator is placed 10 cm past the slit.

Though the monochromator has a mosaicity designed to increase neutrons toward the sample, some will scatter into undesirable directions. A guide channel is placed 30.4 cm away from the monochromator to help redirect some of the monochromatic neutrons scattered but not toward the sample. A Söller linear collimator, characterized by a divergence angle of 11 minutes, is then used to filter out those not traveling in the appropriate direction. Once through the collimator, the beam passes through a slit similar to the one at the end of the previous collimator. The purpose of this slit is to kill any neutrons not headed directly toward the sample reducing noise. The sample is positioned 262 cm away from the monochromator (rotated $2\theta_m$ from the primary beamline direction). An oscillating radial collimator and banana detector setup is used.

2.3.4. Polychromatic Configuration. Using the monochromatized beam, in order to acquire all Bragg angles in the optimum range of scattering angle will require changing the neutron wavelength by rotating the monochromator. Rotation of the monochromator will require an arm to be able to rotate sample table and the banana detector. This can be very challenging in some environments such as those that require high temperatures or a vacuum. Maintaining these environments with minimal additional hardware to reduce excess scatter can be difficult. Polychromatic techniques have been successfully used to alleviate some of these difficulties [47].

In polychromatic wavelength dispersive diffraction, no monochromator is used which allows multiple wavelengths to reach the sample. Since the neutron wavelength is no longer a fixed value, the analyzer which is placed downstream of the sample could be rotated to get different wavelengths to solve Bragg's Equation for the d -spacing, while the diffraction angle, θ_s , must be fixed. The most appropriate angle that which minimizes gauge volume. Gauge volume, illustrated in Figure 2.16, is defined by the intersection of the incident and diffracted beam [47]. For an optimal setup, the irradiated volume should be minimized. This can be achieved by setting θ_s to 45° as the irradiated volume is proportional to $1/\sin(2\theta_s)$ assuming parallel incident and diffracted beams.

In other way, by keeping the analyzer take off angle fixed, the scattering could be rotated where Each 2-theta angle will give different part of powder pattern, which can be combined in refinement stage.

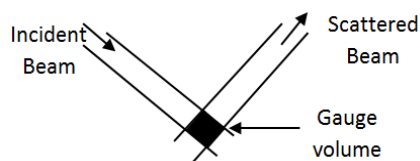


Figure 2.16. Gauge volume.

Therefore, Rotation of analyzer arm combined with changing scattering angle will provide powder pattern in d-spacing. The schematic set up of rotation is shown in Figure 2.17.

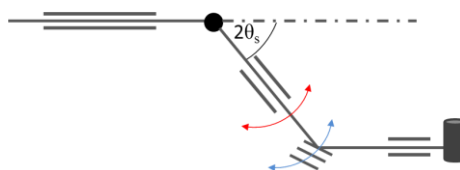


Figure 2.17. The schematic rotation set up for polychromatic configuration

For polychromatic wavelength dispersive diffraction to work effectively, the wavelength of the incident neutrons should be filtered to within a narrow range to remove wavelengths that are not expected to reveal peaks but still contribute to the incoherent background. Simmons recommends using a high energy bandpass X supermirror and low energy bandpass optical filter to remove wavelengths outside $0.6 - 2.9 \text{ \AA}$ [33]. In the Monte Carlo simulation, wavelengths outside this range were simply killed.

In the polychromatic setup, the same monochromatic beamline configuration is used. The monochromator is removed and the sample is placed in its previous location. A Söller linear collimator with divergence of 11 minutes is placed 1.05 m away from the sample. A wavelength sensitive detector is used instead of a banana detector. Figure 2.18 shows the layout of the polychromatic wavelength dispersive diffractometer setup.

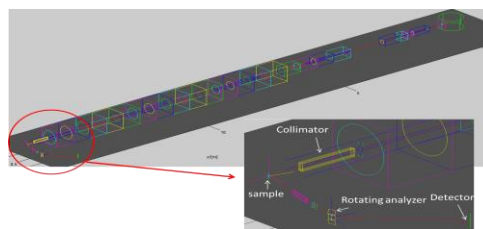


Figure 2.18. The polychromatic layout of NRS beamline.

2.4. RESULTS

For the monochromatic configuration, since the scatter angle θ_s is known and λ_m is constant, the d -spacing of the sample can be computed using Bragg's Equation. Figure 4.1 shows the diffracted peaks of the sample power at different scattering angles in the NRS and D1B configurations. The poor resolution seen in the Figure 2.19 results in the overlapping of the peaks in the higher range of the scattering angle which makes computation of the d -spacing error prone. Though for both, NRS, and D1B, at higher scattering angle the resolution is poorer, for NRS, it is worse.

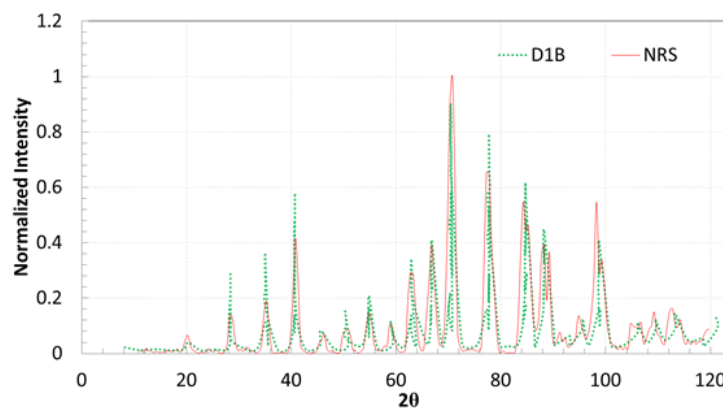


Figure 2.19. The comparison of the diffracted intensity between NRS and D1B.

However, if the peaks can be shifted to the lower scattering angular range by changing the wavelength as shown in Figure 2.20, it is possible to get the optimum

resolution for the peaks of out of ranges. This can be done by polychromatic configuration.

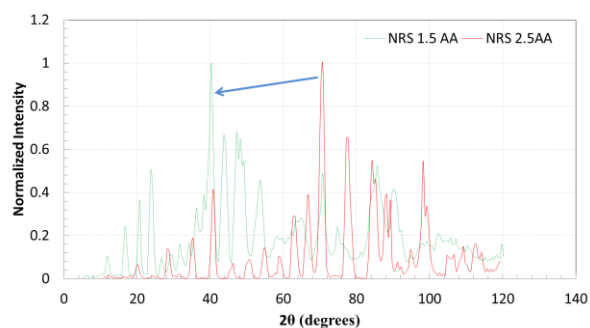


Figure 2.20. The shifting of the peaks by changing the wavelengths.

Table 2.7 shows the calculation of d-spacing for the different wavelengths by changing the analyzer take-off angle while keeping the scattering angle fixed.

Table 2.7. Bragg's peaks for different analyzer takeoff angles

Wavelength (Å)	Bragg plane	d_{Ni} (Å)	$2\theta_s$	$2\theta_A$
2.48	111	2.0345	75°	43.39°
2.15	200	1.7619	75°	37.38°
1.51	220	1.2459	75°	26.02°
1.3	311	1.0625	75°	22.35°
1.24	222	1.0172	75°	21.3°

Figures 2.21 shows the same results that are tabulated in Table 4.1. It shows the diffracted peaks of the sample power at different analyzer take-off angles where

wavelength varies from 1\AA to 3\AA for the variation of the analyzer take off angle from 21.3° to 43.39°

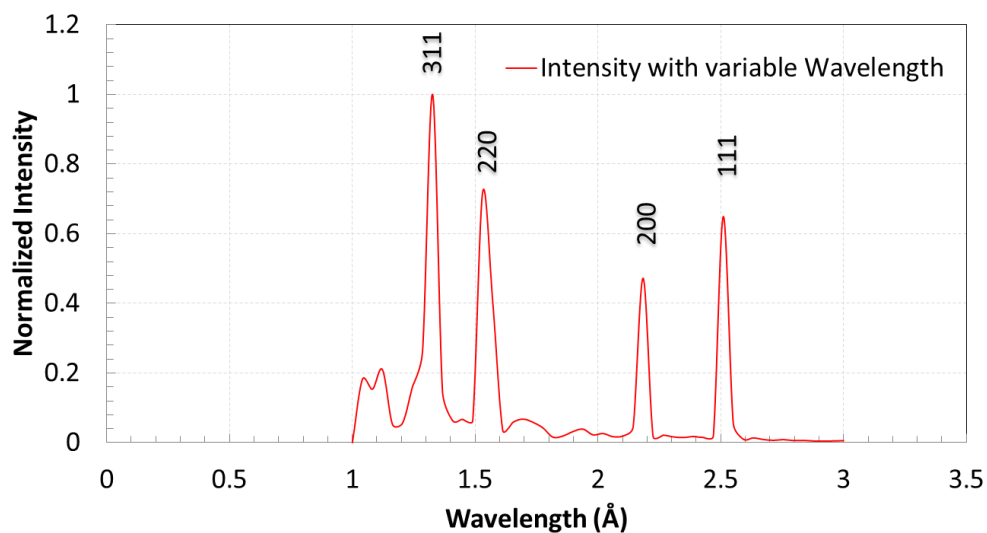


Figure 2.21. The scattered peaks for the variation of wavelengths

The corresponding resolution is shown in the Figure 2.22 where it is clear that at the lower value of the wavelength, higher resolution is achieved compared to the higher values of wavelength.

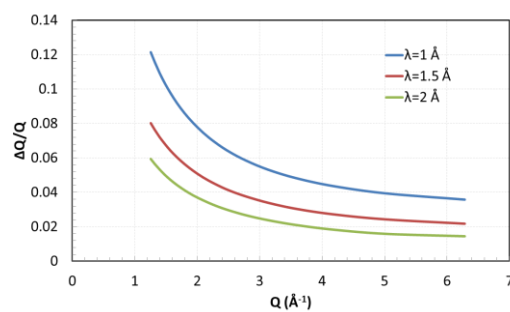


Figure 2.22. The resolution function of wavelengths

On the other hand, while keeping the analyzer takeoff angle fixed and varying the scattering angle would also produce the desired d-spacing values which are shown in the Table 2.8.

Table 2.8. Bragg's peaks for different scattering angles

Wavelength (Å)	Bragg plane	d_{Ni} (Å)	$2\theta_s$	$2\theta_A$
1.5	111	2.0345	43.26°	25.84°
1.5	200	1.7619	50.39°	25.84°
1.5	220	1.2459	74.03°	25.84°
1.5	311	1.0625	89.8°	25.84°
1.5	222	1.0172	95.01°	25.84°

Figure 2.23 shows the graphical results that are tabulated in Table 2.8. It shows the diffracted peaks of the sample power at different scattering angles where the wavelength is fixed at 1.5 Å for the fixed analyzer take off angle of 25.84°.

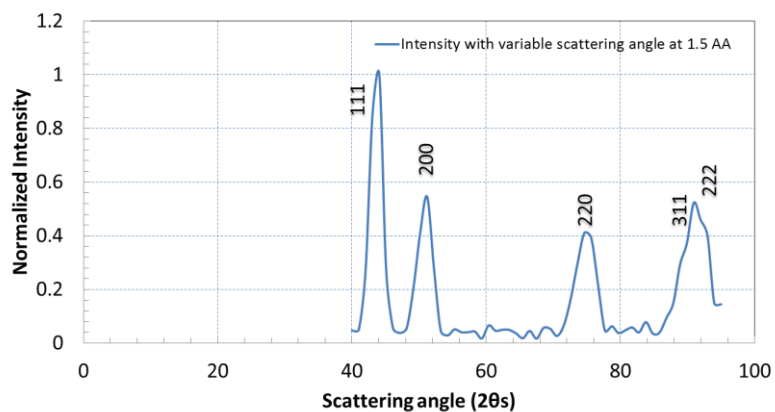


Figure 2.23. The scattered peaks for the variation of scattering angles

The corresponding resolution is shown in the Figure 2.24 where it is clear that the optimum threshold for scattering angle ($2\theta_s$) is 60 for the optimum resolution. Though the peaks for the plane 311 and 222 are overlapped when the scattering angle is varied, they are completely separated when the analyzer take-off angle is varied which implements that the combination of both technique would produce the whole range of d-spacing with good resolutions.

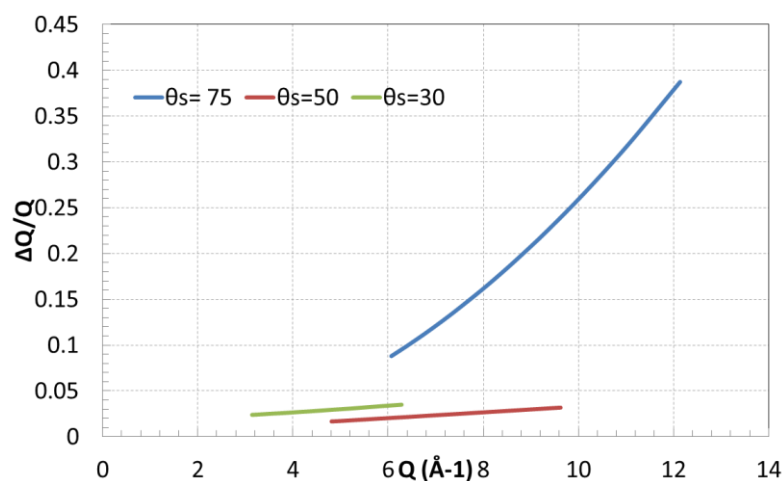


Figure 2.24. The resolution function of scattering angles

It can be concluded that the diffractometer can be designed for single horizontal scattering plane as well as single take-off angle plane. Multiple analyzer-detector channel could be arranged to collect complete diffraction pattern.

3. AUTOMATIC DETECTION OF CARRIES FROM DENTAL X-RAY

3.1. BACKGROUND FOR CARRIES DETECTION

In this section the background of the dental cyst detection is described. The characteristics of the dental cyst are analyzed here in the radiographic digital image.

3.1.1. Dental Carries and Dental Cancer. Oral wellbeing is basic to general wellbeing and personal satisfaction. It is a condition of being free from mouth and facial agony, oral and throat tumor, oral contamination and wounds, periodontal (gum) ailment, tooth rot, tooth misfortune, and different maladies and scatters that point of confinement an individual's ability in gnawing, biting, grinning, talking, and psychosocial prosperity. Around the world, 60–90% of school kids and about 100% of grown-ups have dental cavities. Extreme periodontal (gum) infection, which may bring about tooth misfortune, is found in 15–20% of moderately aged (35-44 years) grown-ups. All inclusive, around 30% of individuals matured 65–74 have no common teeth. According to the Oral Cancer Foundation, nearly 50,000 new cases of oral cancer are expected to be diagnosed this year (2017). Of the new diagnoses, approximately 40% are expected to result in a fatality within the next five years. This severity is not caused by difficulty making an accurate diagnosis or treatment of oral cancer, but rather by late discovery far into the cancer's development [48]. Early detection could reduce the fatality rate by 70% to 90% [49].

3.1.2. Common Methods to Analyze Dental Carries. Early detection of dental cancer is often preceded by the detection of dental caries such as tumors and cysts. Several methods are available for diagnosing dental caries including clinical visual inspection, fiber optic transillumination, bitewing x-ray radiography, caries indication dyes, fluorescent methods, cone beam computed tomography (CBCT), and panoramic x-ray radiography [50]. Amongst these techniques, only radiography methods are applicable for automated lesion detection because they result in an image that can be processed. CBCT produces reliable data but exposes the patient to 10 - 1200 μSv which is far more than the 5 μSv dose acquired from panoramic x-ray radiography [51].

3.1.3. Application of Panaroma Dental X-Ray in Detection Carries. Panoramic dental radiographs, commonly known as orthopantograms (OPGs), are widely used for early diagnosis of oral diseases and facial skeleton injuries. An OPG is a two-

dimensional x-ray image of the entire oral cavity including teeth, surrounding jaw bones, jaw joints, the nasal area, and the sinus cavity [52]. Since this region is optically thin compared to the rest of the human body, a low voltage x-ray tube can be used to achieve good contrast between tissue and bone without requiring contrast agent which enables low dose radiography. The tissue regions in the OPG often suffer from quantum noise but the bone regions are largely unaffected. The quantum noise in the tissue region impedes detection of carries from OPGs [53].

Mapping a 3D structure to a 2D radiograph distorts spatial information and complicates its identification [51]. Identifying structures (object recognition) is crucial for an automated algorithm .

3.1.4. Computer Aided Detection. Object recognition is performed by computer-aided detection (CAD), an automated methodology to help medical specialists identify anomalies from diagnostic tests. High sensitivity can be achieved using CAD [54]. Computerized automatic dental radiography analysis systems for clinical use save time and manual costs and avoid problems caused by intra- and inter-observer variations e.g. due to fatigue, stress or different levels of experience. CAD can be applied to panorama radiography and CBCT images [55]. Furthermore, an automatic method is capable to compare the suspicious or lesion areas against the non-lesion areas in multiple images to identify the closest resemblance. Compared to manual process which is more convenient for identification on a small number of images, an automatic system can be more suitable for the identification on a large database.

3.1.5.Characteristics of the Carries. The periodontium is the specialized tissues surrounding and supporting the teeth, affixing them in the maxillary (upper) and mandibular (lower) jaw bones. Periodontal cysts can be classified into either dentigerous or periapical cysts. Most dentigerous (follicular) cysts are developmental odontogenic cysts evident in adolescents and young adults which is not very common. Periapical (radicular) cysts are the most common type of periodontal cyst. About 60% of periapical cysts are found around a carious incisor or canine [56]. These cysts result from inflammation secondary to caries or other entities and are linked to cancer.

Periapical cysts can be described by their size, shape, location, density, borders, internal architecture, and the effect of adjacent structures. Most periapical cysts are less

than 1 cm in diameter, well-defined, unilocular, radiolucent lesions. They are identified by the radiopaque structures around them. Our methodology is limited to detection of periapical cysts.

3.2. IMAGE PROCESSING AND DETECTION METHODS

In this section some image processing and pattern recognition methods are described that are used to develop the methodology of the proposed method.

3.2.1. Average Intensity Projection. A digital image is represented by a 2D function which is a surface in 3D space. Variation of the intensities of such a surface can be exploited as a curvature with peaks (local maxima) and valleys (local minima) to be detected as important features from images. An analysis of such curvature based peak and valley detection techniques result in identification of the different types of peak and valley positions of the image. Because curvature is a representation of ‘bend’ in the intensity profile along a certain direction of the image, a 1D function is used to analyze the positions of peaks and valleys along that direction. The description of profiles depicted by a peak-valley curvature based technique is the measure of the properties of the average intensity profile of the 1D function [57]. Unlike the traditional peak detection strategy that employs the threshold value of noise coupled with first-order derivative to estimate the peak start and end positions, we emphasize the detection of local maximum points corresponding to underlying peaks. A data point, p_i , represents a local maximum as long as the following equation is satisfied:

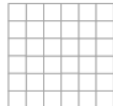
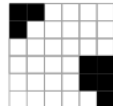
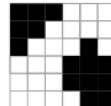
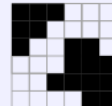
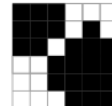
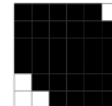
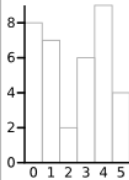
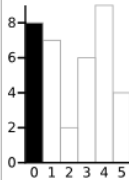
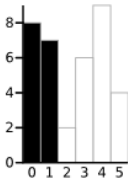
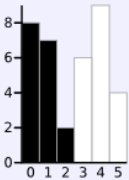
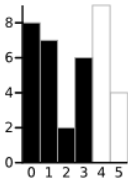
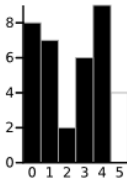






$$p_{i-1} < p_i \text{ and } p_i > p_{i+1} \quad (59)$$

where p_{i-1} and p_{i+1} represent the $i - 1$ th and $i + 1$ th data points, respectively. Similar way the valley is detected as local minima.

3.2.2. Otsu’s Thresholding. Otsu thresholding work better for bimodal or multimodal histogram. It calculated the each class probability, there corresponding mean and variance from which it calculates the within class variance for each of the intensity level of the image. The intensity level which produce the lowest within class variance is

chosen as the threshold value by Otsu's method. Table 3.1 describe the calculation of Otsu's method [58].

Table 3.1. Otsu's thresholding method calculation

Threshold	T=0	T=1	T=2	T=3	T=4	T=5
						
						
						
Weight, Background	$w_b = 0$	$w_b = 0.222$	$w_b = 0.4167$	$w_b = 0.4722$	$w_b = 0.6389$	$w_b = 0.8889$
Mean, Background	$M_b = 0$	$M_b = 0$	$M_b = 0.4667$	$M_b = 0.6471$	$M_b = 1.2609$	$M_b = 2.0313$
Variance, Background	$\sigma_b^2 = 0$	$\sigma_b^2 = 0$	$\sigma_b^2 = 0.2489$	$\sigma_b^2 = 0.4637$	$\sigma_b^2 = 1.4102$	$\sigma_b^2 = 2.5303$
Weight, Foreground	$w_f = 1$	$w_f = 0.7778$	$w_f = 0.5833$	$w_f = 0.5278$	$w_f = 0.3611$	$w_f = 0.1111$
Mean, Foreground	$M_f = 2.3611$	$M_f = 3.0357$	$M_f = 3.7143$	$M_f = 3.8947$	$M_f = 4.3077$	$M_f = 5.000$
Variance, Foreground	$\sigma_f^2 = 3.1196$	$\sigma_f^2 = 1.9639$	$\sigma_f^2 = 0.7755$	$\sigma_f^2 = 0.5152$	$\sigma_f^2 = 0.2130$	$\sigma_f^2 = 0$
Within Class Variance	$\sigma_W^2 = 3.1196$	$\sigma_W^2 = 1.5268$	$\sigma_W^2 = 0.5561$	$\sigma_W^2 = 0.4909$	$\sigma_W^2 = 0.9779$	$\sigma_W^2 = 2.2491$

3.2.3. Gaussian Smoothing Filter. Gaussian smoothing filter is widely used to smooth the image or reduce the noise. It acts as a low pass filter. It uses the Gaussian shaped kernel. Figure 3.1 shows the Gaussian kernel in 2D.

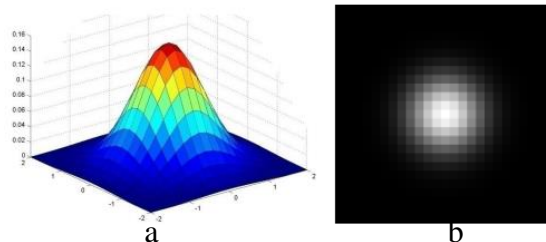


Figure 3.1. Gaussian filter:(a) 3D view (b) the filter displayed as an image

$$G_{\sigma} = \frac{1}{2\pi\sigma^2} e^{-\frac{(x^2+y^2)}{2\sigma^2}} \quad (60)$$

3.2.4. Sobel Edge Detector. Since we want to suppress the high frequency variation in the image, Sobel edge detector is a very good choice to preserve the prominent edges. This operator is used by convolving the image with Sobel horizontal and vertical masks. If the input image is A and the horizontal and vertical masks of Sobel operator is G_x and G_y and the output image is F, the computations are as follows:

$$A_x = G_x * A \quad \text{and} \quad A_y = G_y * A \quad (61)$$

and

$$F = \sqrt{A_x^2 + A_y^2} \quad (62)$$

where

$$G_x = \begin{bmatrix} -1 & 0 & +1 \\ -2 & 0 & +2 \\ -1 & 0 & +1 \end{bmatrix} \quad (63)$$

and

$$G_y = \begin{bmatrix} +1 & +2 & +1 \\ 0 & 0 & 0 \\ -1 & -2 & -1 \end{bmatrix} \quad (64)$$

3.2.5. Erosion Operation. Erosion is one of the most common morphological operation in binary digital image. Erosion shrinks the area of the region of interest. A structural element is used to shrink the region. This process can be analogized to the spatial convolution, though it is not a linear operation like convolution. It is a non-linear process. The structural element is swept over the original image and only those places of the input image having the foreground pixels will be labeled as the foreground pixels of

the output image such that the structural element fits entirely within the shape of the input image. Figure 3.2 (b) shows the eroded image for the erosion of the image of Figure 3.2(a) by the structuring element shown in figure 3.2(c) [59].

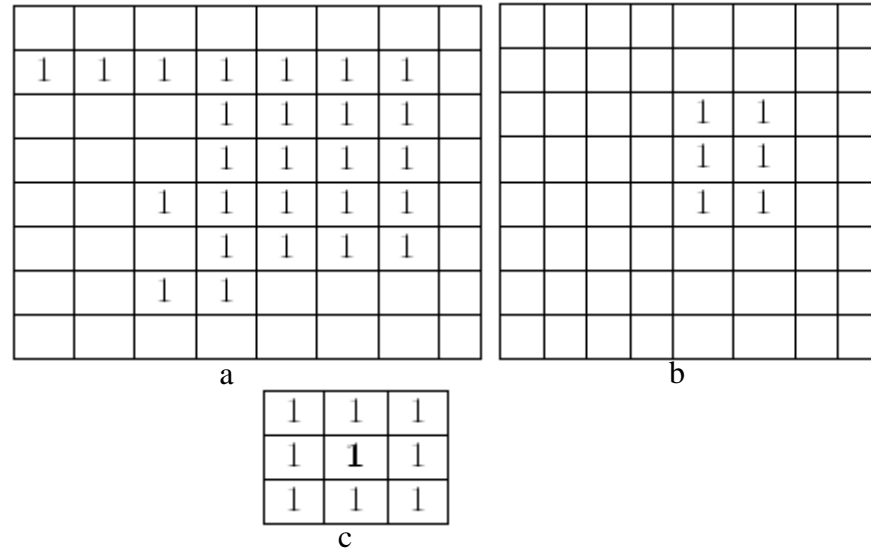


Figure 3.2. Erosion method: (a) binary (b) eroded image, (c) structural element

3.2.6. Row by Row Labelling of Connected Components. Connected component labeling is quite popular method to label the connected regions in binary digital images. If B represents the binary images and (r,c) represents the pixel then values of $B(r,c)$ would be '0' or '1'. The pixels would be connected to each other with respect to their values if there is a sequence of pixels having the same values. The connected path is created by the sequence of pixels. The same label is assigned to all of the connected pixels. The consideration of the connection of the sequence of pixels of same value is made based on either eight neighborhood or four neighborhood definition. In row by row labelling method [60], two scanning passes over the image are made. In the first pass, equivalent labels are recorded and a temporary label is assigned. In the second pass, each of the temporary labels is replaced by the equivalent label. In the Figure 3.3 (b), there are five labels for the connected components for the Figure 3.3 (a). This is the classical method of labelling the connected components.

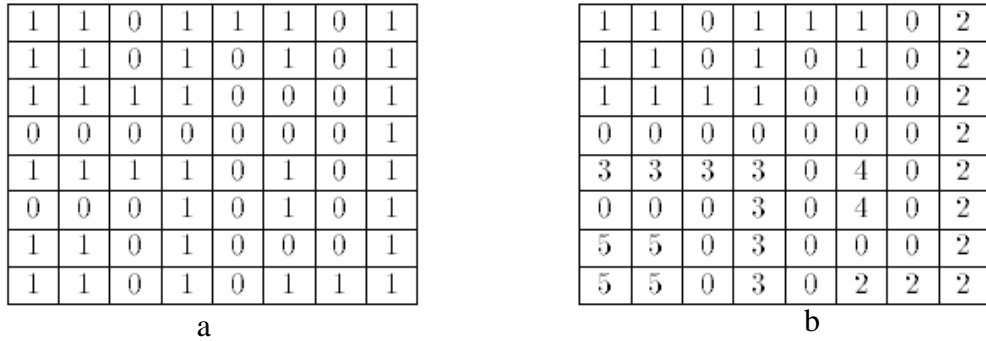


Figure 3.3. Connected components:(a) binary image , (b) labeling.

3.2.7. Region Growing. Region growing plays an important role to segment the region of interest. As the name implies this method basically starts with a seed point and gradually growing the region based on the predefined criteria for extension. The basic approach is attaching to the seed those connecting regions that have the predefined similar characteristics as the seed. Any kind of common information in the ROI, for example range of intensity values, texture and color, can be used as predefined criteria. The process of growing the region would stop when no more pixel will satisfy the criteria to be included [61]. Figure 3.4 shows the important steps of the region growing technique.

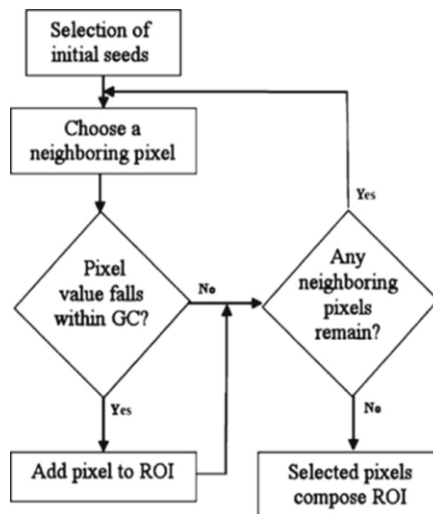


Figure 3.4. Steps of the region growing algorithm.

3.2.8. Feature Extraction. For the analysis of the panoramic X-ray images, one of the essential steps is to extract the important features of ROI. Several works are done on the feature extraction. Shape [52, 62], size [63] and texture morphology [62] of the ROI is considered as some of the important features to extract. Some statistical features, representing the spatial relationship of pixels, of ROI such as brightness [64], homogeneity [65], are also important to define the object. Some features that describe the object in the comparison with the surrounding region are also extracted to differentiate the ROI from other. One of such kind of features could be the ratio of the area of the ROI to the area of the surrounding region [63].

3.2.9. Hough Line Transform. Hough transform is commonly used to detect a line from the aligned points. A polar form representation of line is used here. The Hough transform utilizes this change of representation.

The first step in the Hough transform is to make the input image to a set of edge points. Any kind of edge-detector can be used based on the purpose and the resulting edge image is fed to the Hough process as an input.

The rectangular coordinate positions of the pixels in the edge image are converted to polar coordinate system, i.e. their position is represented using a directional angle θ and a position vector r (distance from the origin in rectangular coordinate) as shown in the Figure 3.5, instead of x and y . (The center of the image is commonly used as the reference point for this change of coordinates.)

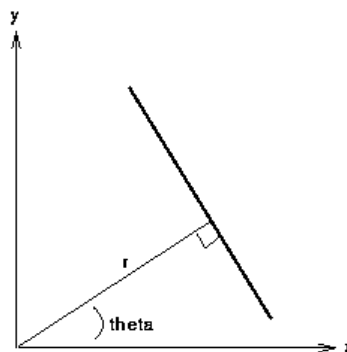


Figure 3.5. The representation of a line

$$x \cos \theta + y \sin \theta = r \quad (65)$$

In an image space or the rectangular coordinate system, the Cartesian (x, y) coordinates of edge pixels are known parameters and hence act as constants in the polar (r, θ) line equation given in equation 64, while r and θ are the unknown variables that need to be determined in order to solve the equation. When all the probable values of (r, θ) defined by each Cartesian point (x_i, y_i) are plotted, points in Cartesian image system are delineated to sinusoidal curves in the polar Hough polar coordinate system. This conversion from *point-to-curve* is named as the Hough transformation for straight lines. Points which are at the same line in the Cartesian image coordinate system produce curves which intersect at a common (r, θ) point in Hough parameter coordinate system.

Quantization of the Hough polar system defined by (r, θ) into finite intervals, formally named as *accumulator cells*, is used to implement this transform. As the algorithm continues, each (x_i, y_i) point is converted to a discretized (r, θ) curve and the accumulator blocks over which this curve is traced are augmented. Consequential peaks in the accumulator cell give the indication that a corresponding straight line presents in the input image [66].

3.2.10. Artificial Neural Network. Artificial neural networks are used to recognize a specific pattern automatically. A neural network is a large parallel networks which are interconnected to each other by a serious of processing units or neurons. The parallel nature of the network enables this system to work faster than the conventional sequential nature of the computation system. A single neuron, performing the core function of the network, takes the weighted the sums of the input and transfer them to the activation function that defines the relationship between the input and the output. The activation function could be the linear or non-linear function depending on the purpose. The weights of the neurons are the parameters that are need be set to define the functionality of the network [67].

The two main categories of neural network is currently available in literature: feed forward neural network and feedback network. Feed forward network is more common. There are connected with multiple layers. The last layer is known as output layer while the

other layers are called hidden layers. The number of neurons in the hidden layers depends on the particular problem. Trial and error method is also widely used to find out the suitable number of neurons for the layers. Of course, more complicated the problem is, more difficult to find out the suitable numbers of neurons. If O_i represents the output of the i^{th} neuron of layer m . the function of the network can be represented by the following equation.

$$O_i^m = f\left[\sum_{j=1}^{N_{m-1}} w_{ij}^{(m,m-1)} y_j^{(m-1)} + \theta_i^{(m)}\right] \quad (66)$$

where $w_{ij}^{(m,m-1)}$ represents the weight from neuron j of layer $m-1$ to neuron i of layer m , $\theta_i^{(m)}$ is the bias of neuron i of layer m . The function f denotes the activation function. The backpropagation learning algorithm is used to train the network so that the network would set the appropriate values of weights and bias in order to map the new pattern to trained pattern as closely as possible.

3.3. DESCRIPTION OF THE ACTUAL WORK

The description of the methodology developed is described in this section. Some literature related to our work are also mentioned here.

3.3.1. Current Status. Since periapical cysts usually occur near specific teeth, the first step in their detection is to identify specific structures such as teeth and the mandible. Active contours are often used to segment cysts and tumors semi-automatically from dental panoramic images [68, 69, 70]. However, active contours require an initial guess for the location (and shape) of the desired feature making them impractical for fully automatic algorithms. Level set segmentation is similarly used to segment features such as cysts from dental panoramas [71, 72] but also requires some initial input to converge accurately.

Another technique that has successfully been used for identification of teeth is integral intensity profile analysis [73]. However, a flaw in integral profile analysis is that

the teeth must have an intact structure. Additionally, integral profile analysis of an entire OPG is difficult so a specific ROI is often selected [74].

Seeded region growing is an automatic process of segmenting the ROI which is free of tuning parameters [61]. To avoid incorrect segmentation, Adams [61] suggests using a region rather than a single pixel. The darkest pixel groups around the teeth are used as the seed region to detect periapical cysts.

Classification of an image (or a segment thereof) is well suited to a neural network classifier. Support vector machines (SVMs) have been used in this capacity successfully [72]. Convolution neural networks have also been used [75].

Recently, Birdal et al. published an algorithm for automatic detection of apical lesions from OPGs. First, they separated the jaws with a wavelet transform and polynomial regression. Then they segmented the teeth and identified the tooth root using angular radial scanning. Finally, they used region growing to find the lesion around the tooth root. They selected the seed point for lesion identification assuming that teeth are darker than gum and lighter than the air gap. They found pixel intensity values along the root detection line and use the first minimum value after the root apex as the seed point if the value is between the intensity values of air gap and gum. They measured specificity and sensitivity to be 89% and 70% respectively [76]. In comparison, the proposed method here achieves similar sensitivity but higher specificity

3.3.2.Data-set. Vatech Humanray Co., Ltd, Korea provided 180 OPGs for statistical analysis and validation of the proposed algorithm. Each image has a resolution of 2776×1504 pixels. Among 180 images, 90 images were randomly chosen for a training set and the rest of the images are used for testing and validation. The proposed algorithm is only valid for OPGs taken with a similar instrument at the same resolution. The detection algorithm was implemented in C++ and OpenCV.

3.3.3. Periodontium Identification. As a whole it is really difficult to analyze the OPG. It is convenient to find out the object of interest from a surrounding smaller region rather than whole image. Therefore, the most prominent structures as shown in Figure 3.6 in the OPG could be used as reference structures from which a smaller region could be deduced to be considered for detail analysis. In OPG the hard palate (shown in Figure. 3.6(a)) is a very prominent structure which is the most horizontal structure and

comparatively brighter. If the position of the hard palate can be detected, the location of the junction of the crown and root, formally known as superior border of alveolar process (shown in Figure 3.6(g)), in the mandible could be easily detected which make the region of analysis smaller. The Hough Transform is used to find out the hard palate. However before using the Hough Transform, the image needs to be preprocessed. To remove noise from the image, a Gaussian smoothing filter is used with a standard deviation size of 20. Then the edges are detected using the simple Sobel edge detector. The edge map, E , is generated from the smoothed image using Eq. 68 where the 3×3 Sobel horizontal (S_x) and vertical (S_y) masks are given in Eq. 67.

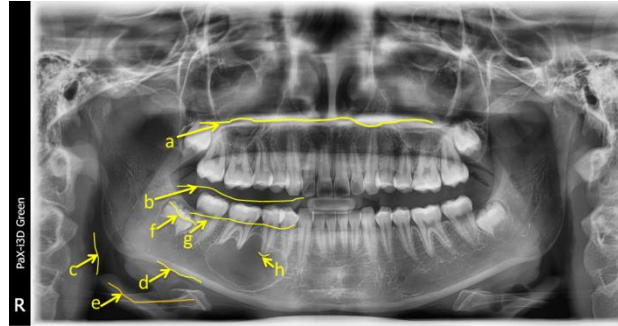


Figure 3.6. Landmarks of panoramic X-rays. (a) hard palate, (b) air gap between upper and lower jaws, (c) oropharyngeal air space, (d) inferior border of mandible, (e) hyoid bone, (f) crown of the tooth, (g) superior border of alveolar process, (h) root of the tooth.

Note that all operations after the convolution are element-wise operations. Figure 3.7 (b) shows the result of convolving the Sobel kernel with the smoothed image shown in Figure. 3.7(a).

$$S_x = \begin{bmatrix} -1 & 0 & +1 \\ -2 & 0 & +2 \\ -1 & 0 & +1 \end{bmatrix} \quad S_y = \begin{bmatrix} +1 & +2 & +1 \\ 0 & 0 & 0 \\ -1 & -2 & -1 \end{bmatrix} \quad (67)$$

$$F = \sqrt{(S_x \otimes ROI)^2 + (S_y \otimes ROI)^2} \quad (68)$$

A threshold is applied to E to produce a binary image as shown in Figure 3.7 (d) using a threshold from the 90th percentile of the histogram of the edge map E to the maximum intensity value as shown in Figure. 3.7 (c). Here the average intensity values are not used because the intensity of the hard palate does not lie within the average intensity range, rather a very distinct range of intensity represents it. This binary image is fed to the Hough transform as an input image to find the most prominent horizontal line, show in Figure. 3.7(d), representative of upper hard palate.

The region below the horizontal line is considered for further analysis. The horizontal integral projection is analyzed in order to find the gap valley between the upper and lower jaws as one of the preliminary steps to detect the junction between the crown and root of the lower jaws. As the gap valley is the most radiolucent area in the considered region, its location would be represented by the lowest valley between two peaks of the profile as shown in Figure 3.8(ii). It is difficult to generalize the position of the junction between the crown and the root if it is detected directly from a bigger region of the image rather than a smaller region achieved step by step. Once the gap valley is detected, the region below it is considered for further analysis.

To remove the region beyond the oropharyngeal air space (shown in Figure 3.6(c)) from both the right and left sides of the image, the vertical integral profile of the region below the gap valley is analyzed. Because the oropharyngeal air space is the predominant air space in the horizontal direction of the region under consideration, it should represent the lowest valley of the profile. However, since the image has a complete black strip with the average intensity of zero just in the beginning of the left border, the second lowest (when the profile starts with zero) and the first lowest valley from the left and right side of the profile respectively are considered as possible locations of the left and right oropharyngeal air spaces as shown in Figure. 3.8(iii). Once the positions of the oropharyngeal air spaces are located, the region within the left and right air spaces would be considered for further analysis which disregards the region outside of them and consequently makes the analysis of detecting the desired object easier and false positive rates lower.

In this discourse, only the left half of the image is discussed now but the rest of the procedure is equally valid when mirrored about the vertical axis. Because of the two comparatively radiopaque (brighter) regions: the inferior border (shown in Figure. 3.6 (d)) and the hyoid bone (shown in Figure. 3.5 (e)) at the bottom of the image, there would be a peak at the bottom of the region in its horizontal profile as shown in Figure.3.8(ii(d)) the nearest valley (Figure. 3.8 (ii(e))) of that peak would be considered as the cutoff threshold, and everything below that point is omitted from further calculation and the initial ROI is produced as shown in Figure.3.8 (iv). The selection of ROI in this way ensures that the teeth roots are preserved while removing the sinus cavity and chin. Other imaging devices or alternative resolutions may require a slightly modified initial ROI depending on the area covered by the imaging system.

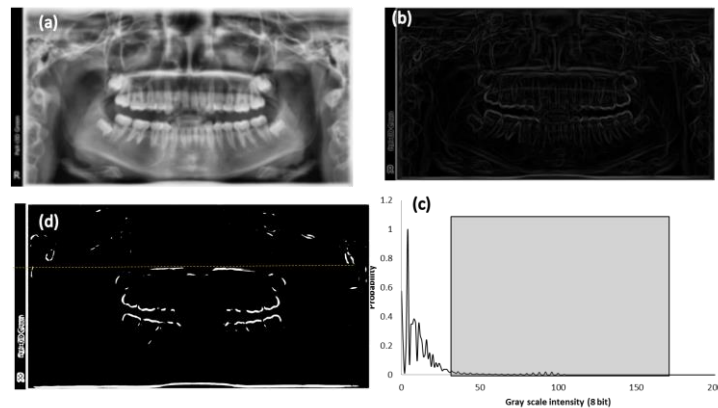


Figure 3.7. Hard palate detection:(a) The smoothed image, (b) edge detected image with Sobel operator, (c) the histogram of image with the region from the 90th percentile to the maximum intensity highlighted, (d) The binary image produced by the highlighted intensity region of (c) with the most horizontal line (dotted) within the image.

The vertical average projection of the ROI (bottom of Figure. 3.9) is used to update the left border of the ROI. The left-most peak in the profile is indicative of the last tooth. In order to identify the peak corresponding to the molar, the profile must be smoothed or noise will be detected as the leftmost peak. To smooth the profile, it is convolved with a normal distribution on $[-3, 3]$ normalized such that the summation is unity.

The magnitude of the smoothing operation is controlled by the number of evaluation points used. We chose 150 evaluation points because that is the approximate width of a typical molar tooth whose identification is sought. Different resolutions should be scaled accordingly. The leftmost peak, x_p , (near x-index = 200 in Figure. 3.9) and local minimum nearest to x_p , x_v , (near x-index = 300 in Figure. 3.9) are identified. The left edge of the ROI, x_L , is computed using Eq. 69.

To remove the region above the mandibular tooth crowns from the ROI, the horizontal integral profile is analyzed. It is smoothed using a Gaussian kernel of the same specifications as previously described. The first valley of two adjacent peaks results from the tooth crown and roots. Therefore, the valley dividing them is the cutoff threshold, and everything above that point is omitted from the ROI.

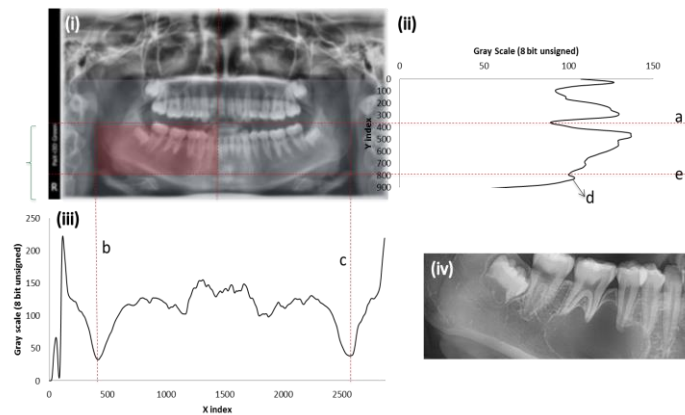


Figure 3.8. Preliminary ROI detection:(i) the smoothed image showing the region below hard palate (light bluish highlighted) and the preliminary ROI (light reddish highlighted), (ii) the horizontal average intensity profile of light bluish highlighted region of (i) where ‘a’, ‘d’ and ‘e’ represent the gap valley between the upper and lower jaws, the inferior mandible border with hyoid bone and the nearest valley of ‘d’ respectively, (iii) the vertical average intensity profile of the region below gap valley where ‘b’ and ‘c’ represent the left and right oropharyngeal air spaces respectively, (iv) the preliminary ROI

$$x_L = \max(0, 2x_p - x_v) \quad (69)$$

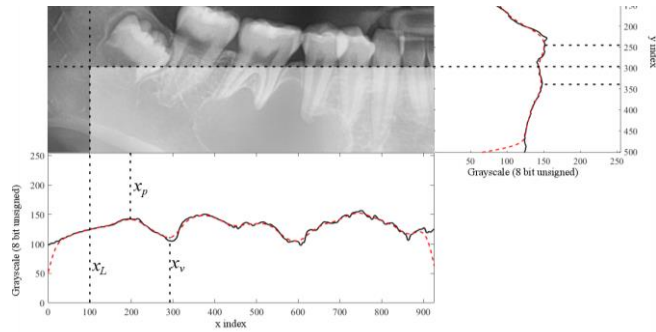


Figure 3.9. An OPG ROI and the average intensity profiles. The smoothed vertical profile (bottom) is used to determine the position of the left ROI boundary. The smoothed horizontal profile showing peaks and valleys (right) is used to determine location of the top ROI boundary. The resulting ROI is highlighted.

The roots are detected using a Sobel edge detector. To remove noise in the image, Gaussian smoothing with a standard deviation of 20 representative to the average tooth length is used. The edge map is generated from the smoothed ROI. Figure 3.10 (a) shows the result of convolving the Sobel kernel with the ROI shown in Figure. 3.9.

A threshold is applied to the edge map to produce a binary image using Otsu's thresholding method [16]. The binary image is shown in Figure 3.10 (b). Artifacts in the binary image are removed using erosion with a 3×3 crossed shape structural element, C , given in Eq. 70. Figure 3.10 (c) shows the new binary image with artifacts removed.

$$C = \begin{bmatrix} 0 & 1 & 0 \\ 1 & 1 & 1 \\ 0 & 1 & 0 \end{bmatrix} \quad (70)$$

Once artifacts are removed, the connected components are computed. The tallest connected component is a result of the longest tooth (usually a bicuspid) which delineates the lowest extent to which the teeth reach. The region below the bottom of this connected component is removed to yield the final ROI. Figure 3.10 (d) shows the tallest connected component (bold box) and the updated ROI (highlighted region).

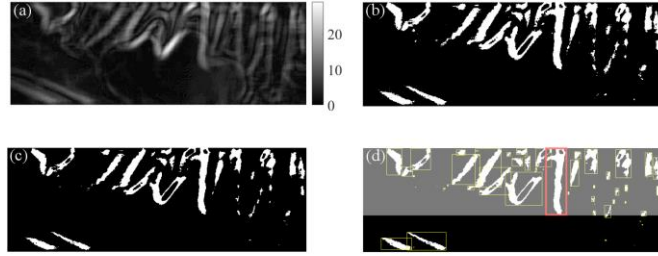


Figure 3.10. Refined ROI detection:(a) Result of convolving a 3×3 Sobel kernel with the ROI (8-bit unsigned image). (b) Binary image obtained from thresholding after convolution. (c) The binary image after artifacts are removed by erosion. (d) The tallest connected component (bold box) is identified and used to update the ROI. The new ROI is highlighted.

3.3.4. Structure Detection. After having the refined ROI, region growing technique is used to determine possible region of probable cyst.

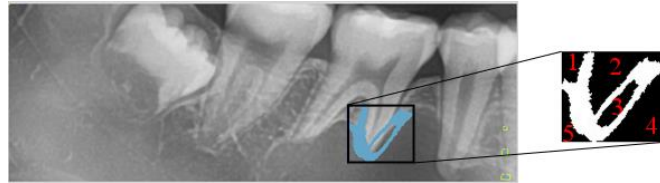


Figure 3.11. Connected component division:a connected component splits the region into different parts. The expanded box shows the different parts identified by connected component analysis inside the connected component's bounding box. The darkest part is the seed region. Here only one connected component is shown because of the clarity of the image.

Each connected component of the final edge image represents an edge between significant structures within the ROI. The region of the original image containing the darkest average pixel value is the seed region for the cyst. Region growing is used to expand the seed region by iteratively expanding the seed region to cover adjacent pixels whose intensity, I , is within a threshold from its minimum intensity, I_{min} , to the 80th percentile I_{80th} of its histogram. Erosion using the kernel defined in Eq. 70 is then applied to the updated seed region to remove any weak linkage created. The exploration

boundary is then expanded. This process continues until the exploration region does not grow. Figure 3.12 shows the region growing methods only for one connected component as an example. Features are extracted and analyzed to determine whether the structure is cystic or benign.

$$I_{\min} < I < I_{80th} \quad (71)$$

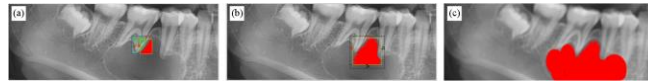


Figure 3.12. Region growing methods. (a) The exploration initialization. (b) An update iteration. The structure (red) expands to include all adjacent pixels within the exploration box that satisfy an intensity threshold. The exploration box is then updated. (c) The final structure identified by region growing when the convergence criteria are met.

3.3.5. Cystic Feature Extraction. After identifying a structure, the size, shape, intensity, and texture are evaluated to compute eight distinct features classifying the structure. The features are then fed into a pre-trained neural network to evaluate whether the structure is cystic.

A shape metric, S , is calculated using Eq. 72 where P is the perimeter of the structure in pixels, and A is its area in total pixels. The scatterness, T , also measures shape, relating the area of the structure to the area of its bounding box, A_r .

$$S = \frac{P^2}{4\pi A} \quad (72)$$

$$T = \frac{A}{A_r} \quad (73)$$

The area of the structure in pixels is used to compute the size relative to the size of the largest cyst found in the randomly chosen training set of ninety images. The area percentage, F is defined in Equation 74 where A_{max} is the largest possible area a cyst was

found to have (12150 pixels). The number of iterations required for the region growing operation to converge, i , is also used as a size metric.

$$F = \frac{A}{A_{\max}} \quad (74)$$

Since cysts have a water-like composition, they should not be excessively radiopaque or radiolucent. Therefore, the average intensity of the structure, I_0 , is extracted as a feature.

Texture is related to the homogeneity of the structure. Holes are groups of connected pixels fully enclosed by the structure but not part of it. Given the number of distinct holes, N_H , T_p is computed using Eq. 75. The difference between the intensity of the holes, μ_H , and the intensity of the rest of the structure, μ_s , reveals the magnitude of the roughness of the structure. This difference, T_q , is computed using Eq. 76.

$$T_p = \frac{N_H}{A} \quad (75)$$

$$T_q = \mu_s - \mu_H \quad (76)$$

Cysts should appear more radiolucent than the surrounding, healthy, tissue. Therefore, two metrics quantifying the relative intensity of the structure relative to its surroundings are included. The first metric, R_U , is the ratio of the average intensity of the region immediately above the structure's bounding box (shown in Figure. 3.13 (a)) to the structure's average intensity. The height of the region above the structure was arbitrarily chosen to be 7 pixels. The second metric, R_O , is the ratio of average intensity inside the structure to the average intensity inside the structure's bounding box but outside the structure itself (see Figure. 3.13 (b)).

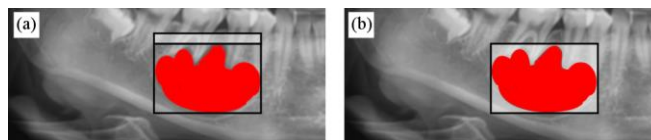


Figure 3.13: The regions that define the ratios RU and RO. Each ratio is the area of the structure (shown in red) to the area of the highlighted region. (a) The upper region. (b) The outer region.

3.4 .RESULTS

One of the most frequent problems that radiologists faces while using CAD software is difficulty in assessing areas of interest due to CAD marks that obscure lesions. Today, most CAD software puts a circle or rectangle over the area of suspicion. The size of this circle or rectangle is usually standard, and does not change from one detection to other. Depending on the size of the mass or calcification in question, the CAD mark obstructs the very area that the radiologist needs to analyze. To allow for easier, more efficient readings for both inexperienced and experienced radiologists, our CAD algorithm developed an upgrading visual aspect of CAD marks in which the mark is assigned as a cross mark shown in Figure 3.14 at nearly the center of the cyst. By this type of representation, the area of suspicion is not obstructed and easily analyzed by the radiologist.

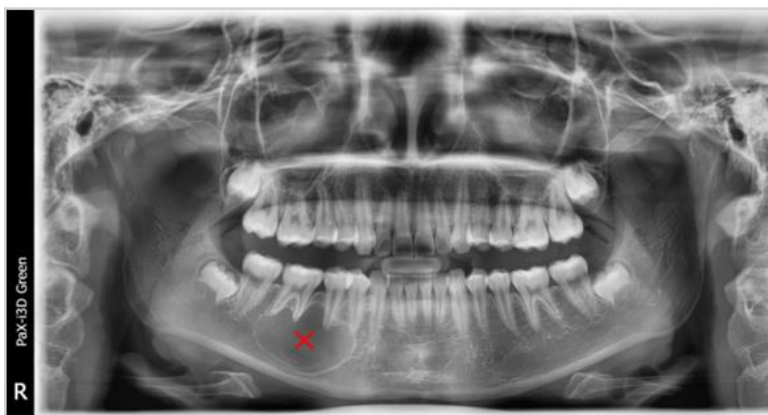


Figure 3.14. Cross mark of the cyst

Currently, the state of the art algorithm for automatic lesion detection is the artificial neural network . However, many images are required to train them [77, 78].

A backpropagation neural network was implemented using the MATLAB Neural Network Toolbox. Figure 3.15 shows the architecture used in this work. The input layer consists of the feature values and bias, B . Each input is multiplied by each weight (W_n) in the hidden layer and summed together. The result (A) is then input to a sigmoid function to produce a binary classification, C , which indicates whether the structure is cystic or non-cystic.

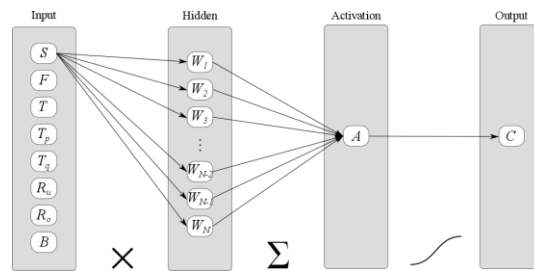


Figure 3.15. The feedforward neural network architecture: all adjacent layers are fully connected.

The neural network was trained using Levenberg-Marquardt backpropagation to compute the optimal weights. The entire data set of 180 OPGs was split randomly into training, validation, and testing datasets. The training dataset contains 90 images with and without lesions while the remaining 90 images are considered for validation and testing, 45 for each. The weights and bias were initialized randomly. Figure 3.16 shows the validation performance during training. The hidden layer has eight (the number of features) nodes. The error function is cross-entropy which ensures that the learning rate is largest when the performance is poorest.

The performance of the algorithm is measured based on three metrics: specificity (precision), sensitivity, and false alarm rate. Sensitivity is a measure of how often the feature is correctly detected. Specificity is a measure of how often lack of a feature is correctly detected. The false positive rate is a measure of the frequency at which a feature is detected but not present in an image. An ideal system would have sensitivity and

specificity of 100% and a false positive rate of 0%. The values obtained from the neural network are given in Table 3.2 using the testing dataset (45 OPGs).

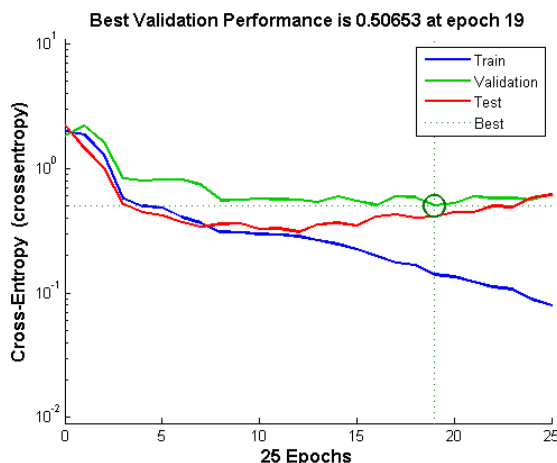


Figure 3.16. The validation performance curve: output by the Matlab Neural Network Toolbox during training.

Table 3.2. Performance criteria

Parameter	Value
Sensitivity	0.90
Specificity	0.87
False Positive Rate	0.013
Average Computation Run Time	22 Seconds

3.5. DISCUSSION AND CONCLUSION

This study presents a novel computer-aided method to detect periapical cysts in the mandible from an OPG. Morphological operations, region growing, and feature extraction methods are developed.

Though this detection method performs well, it is not yet ready for use in a clinical setting as a sole technique for cyst detection. It could be used together with the interpretation of radiologists.

The proposed methodology is limited by the patient's variability in some extreme cases. A larger dataset of sample OPGs could increase the generality of the proposed method to overcome this limitation.

BIBLIOGRAPHY

- [1] Th. Brückel Jülic, “100 Years of Scattering and Beyond,” Lecture Notes of the 43rd IFF Spring School Scattering Methods for Condensed Matter Research: Towards Novel Applications at Future Sources (Forschungszentrum Jülich, 2012).
- [2] Heinz Maier-Leibnitz Zentrum, Neutrons for Research, Industry and Medicine. <http://www.mlz-garching.de/englisch/neutron-research/experimental-methods/elastic-scattering.html>
- [3] D. M. Connor and Z. Zhong, “Diffraction-Enhanced Imaging,” 2014.
- [4] K. Kato, M. Matsumoto, and J. Iwata, “Neutron radiography in vivo imaging of mice and rats.” 1995.
- [5] Abel, M. R., Koltick, D. S. and Nie, L. H. (2016), Associated particle neutron elemental imaging *in vivo*: A feasibility study. *Med. Phys.*, 43: 5964–5972. doi:10.1118/1.4964791
- [6] Geraki K, Farquharson M J and Bradley D A 2002 Concentrations of Fe, Cu and Zn in breast tissue: a synchrotron XRF study *Phys. Med. Biol.* **47** 2327–39
- [7] Mussalo-Rauhamaa H, Piepponen S, Lehto J, Kauppila R and Auvinen O 1993 Cu, Zn, Se and Mg concentrations in breast fat of Finnish breast cancer patients and healthy controls *Trace Elem. Med.* **10** 13–5
- [8] Ng K-H, Bradley D and Looi L-M 1997 Elevated trace element concentrations in malignant breast tissues *Br. J. Radiol.* 375–82
- [9] Rizk S and Sky-Peck H 1984 Comparison between concentrations of trace elements in normal and neoplastic human breast tissue *Cancer Res.* **44** 5390–9
- [10] Santoliquido P, Southwick H and Olwin J 1976 Trace metal levels in cancer of the breast *Surg. Gynecol. Obstet.* **142** 65–70
- [11] Margalioth E J, Schenker J G and Chevion M 1983 Copper and zinc levels in normal and malignant tissues *Cancer* **52** 868–72
- [12] Ghadirian P, Maisonneuve P, Perret C, Kennedy G, Boyle P, Krewski D and Lacroix A 2000 A case-control study of toenail selenium and cancer of the breast, colon, and prostate *Cancer Detect. Prev.* **24** 305–13
- [13] Kato I, Dnistrian A M, Schwartz M, Toniolo P, Koenig K, Shore R E, Zeleniuch-Jacquotte A, Akhmedkhanov A and Riboli E 1999 Iron intake, body iron stores and colorectal cancer risk in women: a nested case-control study *Int. J. Cancer* **80** 693–8

- [14] Nelson R L, Davis F G, Sutter E, Sobin L H, Kikendall J W and Bowen P 1994 Body iron stores and risk of colonic neoplasia *J. Natl Cancer Inst.* **86** 455–60
- [15] Witkowski K, Kozlowski A, Pardela M, Piecuch J and Walichiewicz P 1993 Level of copper in plasma and tissue of patients with esophageal and large bowel cancer *Wiad. Lek.* **46** 586–8 (article in Polish: from translated abstract)
- [16] Xiao K Q and Henderson W J 1992 Electron microscopy microanalysis and quantitative detection of trace elements in carcinoma of the colon *Zhonghua Bing Li Xue Za Zhi* **21** 142–5 (article in Chinese: from translated abstract)
- [17] Banner W P, DeCosse J J, Tan Q H and Zedeck M S 1984 Selective distribution of selenium in colon parallels its antitumor activity *Carcinogenesis* **5** 1543–6
- [18] Gregoriadis G C, Apostolidis N S, Romanos A N and Paradellis T P 1983 A comparative study of trace elements in normal and cancerous colorectal tissues *Cancer* **52** 508–19
- [19] Ogunlewe JO and Osegbe DN 1989 Zinc and cadmium concentrations in indigenous blacks with normal, hypertrophic, and malignant prostate *Cancer* **63** 1388–92
- [20] Chirulescu Z, Chiriloiu C, Suciuc A, Pirvulescu R and Gh N 1987 Variations of zinc, calcium and magnesium in normal subjects and in patients with neoplasias *Med. Interne* **25** 257–61
- [21] Bataineh Z M, Bani Hani I H and Al-Alami J R 2002 Zinc in normal and pathological human prostate gland *Saudi Med. J.* **23** 218–20
- [22] Brys M, Nawrocka A D, Miekos E, Zydek C, Foksinski M, Barecki A and Krajewska W M 1997 Zinc and cadmium analysis in human prostate neoplasms *Biol. Trace Elem. Res.* **59** 145–52
- [23] Zaichick V Ye, Sviridova T V and Zaichick S V 1997 Zinc in the human prostate gland: normal, hyperplastic and cancerous *Int. Urol. Nephrol.* **29** 565–74
- [24] Picurelli L, Olcina P V, Roig MD and Ferrer J 1991 Determination of Fe, Mg, Cu, and Zn in normal and pathological prostatic tissue *Actas Urol. Esp.* **15** 344–50
- [25] Feustel A, Wennrich R and Dittrich H 1989 Investigations of trace elements in metastases and primary carcinoma of the prostate *Urol. Res.* **17** 107–9
- [26] Romics I and Katchalova L 1983 Spectrographic determination of zinc in the tissues of adenoma and carcinoma of the prostate *Int. Urol. Nephrol.* **15** 171–6

- [27] Habib F K, Hammond G L, Lee I R, Dawson J B, Mason M K, Smith P H, Stitch S R Y K, Meade A G, Rack E P and Blotcky A J 1976 Metal-androgen interrelationships in carcinoma and hyperplasia of the human prostate *J. Endocrinol.* **71** 133–41
- [28] Platz E A, Helzlsouer K J, Hoffman S C, Morris J S, Baskett C K and Comstock G W 2002 Prediagnostic toenail cadmium and zinc and subsequent prostate cancer risk *Prostate* **52** 288–96
- [29] Kubo H, Hashimoto S and Ishibashi A 1976 Simultaneous determinations of Fe, Cu, Zn, and Br concentrations in human tissue sections *Med. Phys.* **3** 204–9
- [30] L. Liang et al. (eds.), *Neutron Applications in Earth, Energy and Environmental Sciences*, Neutron Scattering Applications and Techniques, DOI 10.1007/978-0-387-09416-8_2, c Springer Science+Business Media, LLC 2009
- [31] V. K. Pecharsky and P. Y. Zavalij, *Fundamentals of Powder Diffraction and Structural Characterization of Materials*, Kluwer Academic Publishers, Boston, 2003.
- [32] Vladimir Pomjakushin, AIC Information Day on “Large Facilities for Crystallography Studies: Synchrotron and Neutron sources” October 19th, 2009 , Paul Scherrer Institut, Villigen, Switzerland
- [33] J. M. Simmons, J. C. Cook, R. M. Ibberson, C. F. Majkrzak and D. A. Neumann. “Polychromatic Energy-Dispersive Neutron Diffraction at a Continuous Source,” *Journal of Applied Crystallography* **46**. 2013. pg 1347-1352
- [34] A. Martin, B. Paul, C.K. Jeremy, D. Huub, “Powder Diffraction on the WEB,” Department of Chemistry, Christopher Ingold Laboratories, UCL, 20 Gordon Street, London WC1H 0AJ, United Kingdom.
- [35] V.Garlea, B. Chakoumakos ,S. Moore ,G. Taylor ,T. Chae, R. Maples ,R.Riedel ,G. Lynn and D. Selby, “The high-resolution powder diffractometer at the high flux isotope Reactor”, *Appl. Phys.* , pp. 531-535, 2010
- [36] Department of Physics and Astronomy, University of Missouri Columbia. http://web.missouri.edu/~montfroi/jw/neutrons/neutron_scattering/tb/components/monochromator.html
- [37] Neutron Powder Diffraction Facility, NCSU. <http://www.ne.ncsu.edu/nrp/npdf.html>
- [38] A. W. Hewat: *Nucl. Inst. Methods* **127** 361 (1975)
- [39] Hewat, A. W., "Neutron Powder Diffraction on the III High Flux Reactor and High TC Superconductors," *Materials and Crystallographic Aspects of HTc Superconductivity*, 1994, Springer Netherlands, 17-44.

- [40] Sarah W. Morgan, Jeffrey C. King, and Chad L. Pope. "Beam Characterization at the Neutron Radiography Reactor," *Nuclear Engineering and Design* **265**. 2013. pg 639-653.
- [41] L. D. Cussen, and K. Lieutenant. "Computer simulation tests of optimized neutron powder diffractometer configurations," *Nuclear Instruments and Methods in Physics Research A*. **822**. 2016. pg. 97–111.
- [42] Peter Willendrup, Uwe Filges, Lukas Keller, Emmanuel Farhi, and Kim Lefmann. "Validation of a realistic powder sample using data from DMC at PSI," *Physica B: Condensed Matter*. **385–386**, Part 2. 15 November 2006. pg. 1032–1034.
- [43] S. E. Nagler, W. T. Lee, and R. Moon. "Design and simulation of the CG1 beamline at HFIR," *Applied Physics A*. **74** (Suppl 1) 2002. pg. s1495-s1497.
- [44] G. R. J. Artus, R. Gilles, F. Frey, and W. Scherer "Concept of the new thermal single crystal diffractometer at FRM-II," *Physica B: Condensed Matter* **276–278**, March 2000, pg. 77–78.
- [45] G.R. Imel, G. C. McClellan, and D. P. Pruett. "The Neutron Radiography Reactor (NRAD)," The First International Topical Meeting on Neutron Radiography System Design and Characterization. Aug. 28-30 1990. Pembroke, Canada.
- [46] Leo D. Cussen, "Optimizing constant wavelength neutron powder diffractometers," *Nuclear Instruments and Methods in Physics Research A*. **821**. 2016. pg. 122–135.
- [47] Aaron M. Percival, "The White Beam Steady-State Diffractometer: A Next Generation Neutron Diffraction Strain Scanner," (Master's thesis). Queen's University (2009).
- [48] M. D. Mignogna, S. Fedele, L. Lo Russo "The World Cancer Report and the burden of oral cancer," *Eur J Cancer Prev*. 2004 Apr; 13(2): 139–142.
- [49] David A. Mitchell, Anastasios N. Kanatas, *An Introduction to Oral and Maxillofacial Surgery*, CRC Press, 2014.
- [50] M. Z. Booshehry, H. Fasihinia, M. Khalesi, L. Gholami, "Dental Caries Diagnostic Methods," *DJH* **2**(1) 2010.
- [51] L. Grafova, M. Kasparova, S. Kakawand, A. Prochazka, T. Dostalova, "Study of Edge Detection Task in Dental Panoramic Radiographs," *Dentomaxillofacial Radiology* **42**(7), 2013.
- [52] Pedro Lira, G. A. Giraldo, L. A. P. Neves, "Segmentation and Feature Extraction of Panoramic Dental X-ray Images," *Nature-Inspired Computing Design, Development, and Applications*. 2012, Ch 17.

- [53] Andre Gahleitner, G. Watzek, and H. Imhof, "Dental CT: imaging technique, anatomy, and pathologic conditions of the jaws," *European Radiology* **13**(2), Feb. 2003. pp 366-376.
- [54] Ronald A Castellino, "Computer aided detection (CAD): an overview," *Cancer Imaging* **5**(1), 2005, pp. 17-19.
- [55] S. Galib, F. Islam, M. Abir, H. K. Lee, "Computer aided detection of oral lesions on CT image," *Journal of Instrumentation* **10**, Dec. 2015.
- [56] S. C. White, M. J. Pharaoh, *Oral Radiology: Principles and Interpretation*, 4th ed. St Louis: Mosby, 2000.
- [57] S. Chandra and J. Sivaswamy, "An Analysis of Curvature Based Ridge and Valley Detection," IEEE International Conference on Acoustics Speech and Signal Processing Proceedings, 2006, 2, II-II
- [58] O. Nobuyuki (1979), "A threshold selection method from gray-level histograms". *IEEE Trans. Sys., Man., Cyber.* **9** (1): 62-66
- [59] S. R. Sternberg, "Grayscale Morphology," Computer Vision, Graphics, and Image Processing, Vol. 35, 1986, pp. 333-355.
- [60] R. Lumia, .G. Shapiro, and O. Zuniga, "A New Connected Components Algorithm for Virtual Memory Computers," Computer Vision, Graphics, and Image Processing, Vol. 22, 1983, pp. 287-300.
- [61] R. Adams, L. Bischof, "Seeded region growing," IEEE Transactions on Pattern Analysis and Machine Intelligence, Vol, 16, No. 6, June 1994,pp. 641-647
- [62] R. S. Chora's, Image Feature Extraction Techniques and Their Applications for CBIR and Biometrics Systems, International Journal of Biology and Biomedical Engineering, Issue 1, Vol. 1, 2007
- [63] J.P. Thiran, B.Macq, "Morphological feature extraction for the classification of digital images of cancerous tissues," IEEE Transactions on biomedical engineering 43 (10), 1011-1020
- [64] B.Vijayakumari, G.Ulaganathan, A. Banumathi, A.Farzana Shahar Banu, M. Kayalvizhi, Dental Cyst Diagnosis using Texture Analysis, 2012 IEEE
- [65] Jincy Raju, Chintan K Modi, A proposed feature extraction technique for dental X ray images based on multiple features, International Conference on Communication Systems and Network Technologies, IEEE Xplore, 2011.

- [66] J. Illingworth, J. Kittler, "A survey of the Hough transform," *Comput. Vis. Graph. Image Process.* 44(1), 87–116 (1988)
- [67] M. Alwakeel, and S. Zyad, "Face recognition based on Haar wavelet transform and principal component analysis via Levenberg-Marquardt backpropagation neural network." *European Journal of Scientific Research* 42.1 (2010): 25-31.
- [68] T. Matsumoto, T. Hayashi, T. Hara, H. Fujita, "Automated scheme for measuring mandibular cortical thickness on dental panoramic radiographs for osteoporosis screening," *Proceedings of SPIE – The International Society for Optical Engineering*. Feb. 2012.
- [69] I. Nurtanio, I. K. E. Purnama, M. Hariadi, M. H. Purnomo, "Cyst and Tumor Lesion Segmentation on Dental Panoramic Images using Active Contour Models," *IPTEK* 22(3), 2011.
- [70] J. Oliveira, Hugo Proença, "Caries Detection in Panoramic Dental X-ray Images," J.M.R.S. Tavares and R.M.N. Jorge (eds.), *Computational Vision and Medical Image Processing: Recent Trends, Computational Methods in Applied Sciences 19*, Springer Science+Business Media B.V. 2011
- [71] P. L. Lin, P. Huang, P. Huang, "An Automatic Lesion Detection Method for Dental X-ray Images by Using Segmentation Using Variational Level Set," *Proceedings of the 2012 International Conference on Machine Learning and Cybernetics*, Xian, July 15-17 2012.
- [72] Shuo Li, T. Fevens, A. Kryzak, C. Jin, S. Li, "Semi-automatic Computer Aided Lesion Detection in Dental X-rays Using Variational Level Sets," *Pattern Recognition* 40 (10), 2007, pp. 2861-2873.
- [73] S. Valizadeh, M. Goodini, S. Ehsani, H. Mohseni, F. Azimi, H. Bakhshandeh, "Designing of a Computer Software for Detection of Approximal Carries in Posterior Teeth," *Iran Journal of Radiology*, 12 (4) Oct. 2015.
- [74] D. Frejlichowski, R. Wanat, "Automatic Segmentation of Digital Orthopantomograms for Forensic Human Identification," *ICIAP 2011. Lecture Notes in Computer Science*, vol 6979. Springer, Berlin, Heidelberg
- [75] Hyunjun Eun and Changick Kim, "Oriented tooth localization for periapical dental X-ray images via convolutional neural network," 2016 Asia-Pacific Signal and Information Processing Association Annual Summit and Conference (APSIPA). Dec. 2016.
- [76] R. G. Birdal, E. Gumus, A. Sertbas, I. S. Birdal, "Automated Lesion Detection in Panoramic Dental Radiographs," *Oral Radiology* 32 (2) 2016 pp. 111-118.

[77] S. Zhenghao , H. Lifeng, S. Kenji , N. Tsuyoshi and I. Hidenori, “Survey on Neural Networks Used for Medical Image Processing,” *International Journal of Computational Science* **3** (1), Feb. 2009, pp. 86–100.

[78] S. William, M. Randy, S. Joe, C. Xiaohe, G. Kapil, N. Ravirala, S. Bijaya, J. Pavani, “Automatic Detection of Critical Dermoscopy Features for Malignant Melanoma Diagnosis,” U. S. Patent 20060269111 A1, issued Nov 30, 2006.

VITA

Fahima Fahmida Islam was born on October, 1987, in Dhaka, Bangladesh. She received her Bachelor of Science in Civil Engineering from Bangladesh University of Engineering and Technology, Dhaka, Bangladesh in October 2010. After graduation, being a part of researcher, she joined to Missouri University of Science and Technology (Missouri S&T) for pursuing her M.S. in Nuclear Engineering. She pursued her PhD after finishing her M.S.

Fahima held a Graduate Research Assistantship under Dr. Hyoung Koo Lee with the department of Nuclear Engineering at Missouri S&T. She received her Master of Science in Nuclear Engineering from Missouri University of Science and Technology in December 2013, and her PhD in Nuclear Engineering from Missouri University of Science and Technology in July 2017.